Nature of The Soft Excess in Blazar 3C273

by

Shayaan Sajid

A THESIS SUBMITTED IN PARTIAL FULFILMENT OF
THE REQUIREMENTS FOR THE DEGREE OF

BACHELOR OF SCIENCE

in

Honours Astrophysics

(Department of Astronomy and Physics, Dr. Luigi C. Gallo supervising faculty)

. . . .

. . . .

. . . .

. . . .

. . . .

SAINT MARY'S UNIVERSITY

May 20, 2020

ABSTRACT

The multi-epoch data involving 27 observations of the blazar 3C273 obtained over a period of 16 years from June 2000 to June 2016 in the 0.3-10 keV x-ray band is analysed. A single power-law model is fitted to the hard x-ray band while a double power-law model is fitted to the 0.3-10 keV band. The soft x-ray band in 0.3-0.8 keV range is observed to be originating in the jet due to synchrotron self-Compton (SSC) effect while the hard x-ray band is also observed to be originating in the jet through the external Compton (EC) effect. Furthermore, the accretion rate of 3C273 is found to be increasing with time while the jet power has been observed to be decreasing with time.

NATURE OF THE SOFT EXCESS IN BLAZAR 3C273

by *Shayaan Sajid*

submitted on May 20, 2020:

Contents

List of Figures

List of Tables

Chapter 1

INTRODUCTION

1.1 AGN AND THE UNIFIED MODEL

The active galactic nuclei (AGN) observed in the center of galaxies consist of supermassive black holes with masses ranging from about $10^6\ M_\odot$ to $10^{10}\ M_\odot$. These black holes have been observed to be constantly accreting material from their surroundings and are therefore considered as active. Due to this accretion and other physical processes, AGN emit vast amounts of energies in the form of radiation in all wavebands. The luminosity of an AGN can range from about 10^{43} to 10^{49} erg s^{-1} which is emitted from different regions due to different physical processes taking place in those regions. A typical active nucleus mainly has the following regions and components:

- Supermassive black hole at the center
- A hot corona consisting of ionized material mostly electrons
- An accretion disk
- Broad Line Region (BLR)
- Narrow Line Region (NLR)
- A thick cloud of gas and dust known as the torus
- An elongated jet

Since there are a number of different classes of AGN with different spectral features

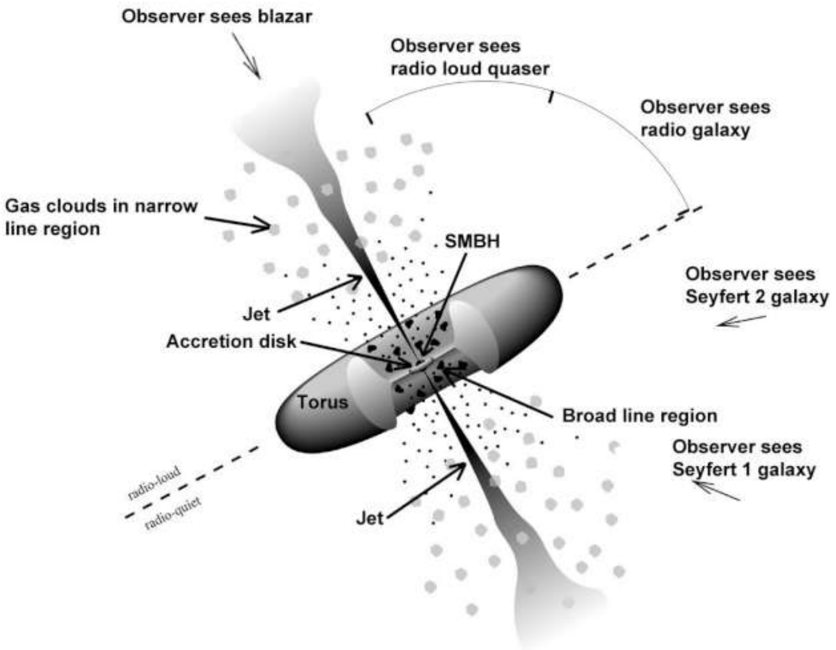

Figure 1.1: The unified model based on the orientation of the AGN. The angle of inclination determines the class of the AGN and the physical processes such as relativistic beaming and obscuration that will affect the spectral features observed in those classes. Image Credit:`https://fermi.gsfc.nasa.gov/science/eteu/agn/`

that have been observed over the years, astronomers have come up with unification schemes that could explain all the different physical processes that are observed in these objects. However, even though there are still many missing pieces in a complete understanding of them, the unified model of AGN that has been built so far is mainly based on the assumption that all the observed different classes of AGN are intrinsically the same but are observed at different viewing angles (Urry and Padovani, 1995) as depicted in Fig. 1.1 above.

1.1.1 THE CORONA

The corona is believed to be the inner, hottest region of AGN that lies near the black hole surrounding the inner side of the accretion disk in some geometry. The region mostly consists of hot plasma of electrons and probably other ionized material from the disk. Its complete structure in not fully understood, but more recently, astronomers discovered that its height above the black hole varies on a timescale of days (Alston et al, 2020). Apart from its structure, the region lies above the accretion disk, and therefore when the UV and soft x-ray photons ($< 2\,\text{keV}$) are emitted from the disk and collide with the energetic electrons in the corona, they are up-scattered to hard x-ray photons ($> 2\,\text{keV}$) through inverse Compton scattering (Sect. 1.3). The up-scattered photons escape the corona isotropically to travel in different directions, some of them illuminate the disk and therefore produce a reflection spectrum from the disk.

1.1.2 THE ACCRETION DISK

The accretion disk is typically the most luminous component in AGN. The supermassive black hole at the center accretes gas and dust from the surrounding galaxy. The surrounding gas and dust arrange in a planar accretion disk around the black hole because of the conservation of angular momentum. The black hole and the accretion disk co-rotate in the same plane because when the matter from the planes inclined at different angles collide in the plane of intersection, their angular momenta combine, and thus the matter eventually comes to orbit in only one plane as shown in Fig. 1.2.

The planar disk formed can have a radius from 100 to 1000 times the Schwarzschild radius, and the matter in the accretion disk follows Keplerian orbits (Rosswog and

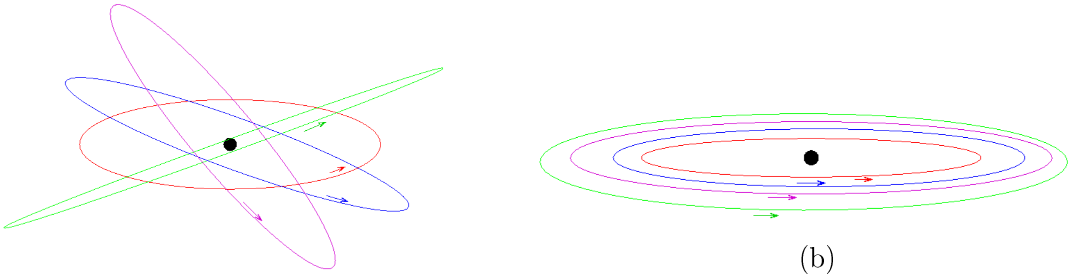

(a)

(b)

Figure 1.2: The formation of accretion disk where a) the incoming matter is inclined at different planes, and b) then falls into one plane after collisions. Image Credit:http://spiff.rit.edu/classes/phys240/lectures/blackholes/blackholes.html

Bruggen, 2007). The accreted material then heats up due to collisions/friction within the disk and moves in towards the black hole. The accretion disks emit vast amount of energy in the form of blackbody radiation (Sect. 1.3).

1.1.3 BROAD-LINE REGION (BLR)

The Broad-line region lies between the accretion disk and the thick torus as shown in Fig. 1.1 with a distance of about 0.001-0.01 pc from the black hole. The optical/UV spectra obtained from this region of the AGN consist of broad, permitted emission lines which are believed to originate due to the photoionization in the region. This is because the regions have high electron number densities with $n_e > 10^9 \text{cm}^3$ (Peterson, 2006) and therefore the photons from the strong, continuum emission from the accretion disk must be ionizing the atoms of the gas in the region, resulting in high electron number densities. These electrons upon recombination with the ions emit broad emission lines that have widths corresponding to velocities that range from about 1000 to 25000 km s^{-1}. These broad line widths can be explained by the

Doppler effect from the bulk motion of the gas clouds in the region.

1.1.4 NARROW-LINE REGION (NLR)

Unlike broad-line regions, the narrow-line regions have low number densities of electrons. They lie outside the plane of the AGN at distances that range from 10 kpc to 100 kpc from the center as shown in Fig. 1.1, and their plane is roughly perpendicular to the plane of the AGN. However, the main difference between the BLRs and NLRs is that the emission lines coming from the narrow line regions are forbidden lines. That is, they correspond to the atomic transitions between the energy levels that cannot occur according to the quantum mechanical selection rules. Hence, this suggests a low density of the gas in the region (Braito et al, 2017) and so less collisions between the atoms can occur. Apart from the transitions, the widths of the lines are narrower compared to BLR lines with values around 500 km s^{-1} (Peterson, 2006).

1.1.5 THE TORUS

The torus is a thick cloud of molecular gas and dust which has an inner radius of about 1 pc from the center of AGN. As for the outer radius, the extent of the torus differs in Seyfert galaxies, and therefore it is not yet completely understood as to how far out the cloudy region extends. High resolution infrared observations now suggest that the outer radius of the torus is no more than few parsecs (Elitzur, 2008) whereas before the outer radius was believed to be hundreds of parsec. This uncertainty is mainly because of the complicated axysymmetric, toroidal structure of the cloud. Compared to other regions of the AGN, the torus is relatively cooler with inner temperature around 800 K and the outer temperature around 320 K (Schartmann et al, 2005), and its emission peaks in the infrared region with a blackbody spectrum. As can be seen from Fig. 1.1, it is the obscuration of the BLR by the thick torus that is responsible for the differences observed in Seyfert 1 and Seyfert 2 galaxies since the radiation coming from the inner region is absorbed by the cloud.

1.1.6 THE JET

As shown in Fig. 1.1, the elongated jet lies perpendicular to the plane of the AGN. AGN observed to be consisting of jets are called quasars since their emission peaks in radio wavelengths. The two lobes of the jets are pointing in opposite directions and are about 10^5 pc in length. A number of quasars that have been observed over the years are highly redshifted with redshifts above 6, and they are observable even with such enormous distances because they are the most luminous objects in the Universe. However, it is not completely understood how the jets form but their formation is believed to be related to the magnetic field and spin of the black hole (Sect. 1.2.1).

1.1.7 THE UNIFYING MODEL

Based on the description of the components of AGN above and their depiction in Fig. 1.1, two unification schemes have been made to give a unified model of the AGN. The first one is based on the radio observations of AGN to explain the differences between blazars, radio-loud quasars, and radio galaxies where the radio emission is strong but not as strong as blazars. As mentioned earlier, the differences between different classes of AGN occur due to different inclination angles. If the jet of the AGN is pointing directly in the line of sight of the observer, then it is classified as a blazar which is one of the most luminous radio sources in the Universe. However, if the jet is not pointing in our line of sight, but is still inclined towards the Earth, then it becomes the second most luminous radio source known as quasar. If the jet is not oriented towards Earth and lies more in the plane of the sky, then it is classified as a radio galaxy. The physical process responsible for making the quasars more luminous in radio wavelength than the radio galaxies is relativistic beaming (Sect. 1.3).

The second unification scheme is based on the observations made in the optical and infrared band. It classifies the AGN into Seyfert 1 Galaxies and Seyfert 2 Galaxies as shown in Fig. 1.1, and the physical process responsible for the differences in these two classes is the obscuration by the torus. As mentioned earlier, the torus is a cloud of molecular gas and dust that encloses the inner region of the AGN. Due to this, the ionizing radiation coming from the inner region is blocked by the cloud, and therefore, if viewed edge on, the luminous regions such as the accretion disk and BLR are obscured by the cloud resulting in a relatively low luminosity class of AGN known as Seyfert 2 galaxies. The emission lines that we do see from Seyfert 2 correspond to the narrow line regions. On the other hand, if we observe the AGN at an angle where the region between the torus and the accretion disk becomes visible, then we observe the broad emission lines of the region resulting in a higher luminosity galaxy classified as a Seyfert 1 galaxy.

These models have been shown to agree in the few cases where we have observed both the jet and the BLR visible at the same time. While this unified model has a strong observational support, many radio-quiet AGN that have been observed in the recent years seem to possess no jet, and their spectra is mostly dominated by the emission from the accretion disk.

1.2 JETTED AGN

Accroding to the unified model, the jets of radio-loud sources classify as either quasars or blazars depending on the angle of inclination. However, blazars can be further classified into two sub-classes which are known as Flat-Spectrum Radio Quasars (FSRQ) and BL Lacertae objects, and the difference between them is due to their spectra. The spectra of FSRQs have their synchrotron emission peaked at lower frequencies and BL Lacertae objects have their synchrotron emission peaked in the UV or X-ray band (Bhatta et al, 2018).

Despite the differences in their spectra, all blazars show high variability in their spectra on timescales of days to years, and their spectra is mostly dominated by the jet. The jets of all blazars are believed to consist of a helical magnetic field coiled around an ionized plasma that is propelled outwards perpendicularly from the center and traveling at relativistic speeds (Marscher, 2016). Although a complete physical model to explain the presence of jets in AGN is still in the works, the model that provides the most accurate description so far is the Blandford-Znajek Model (Blanford and Znajek, 1977).

1.2.1 BLANDFORD-ZNAJEK MECHANISM

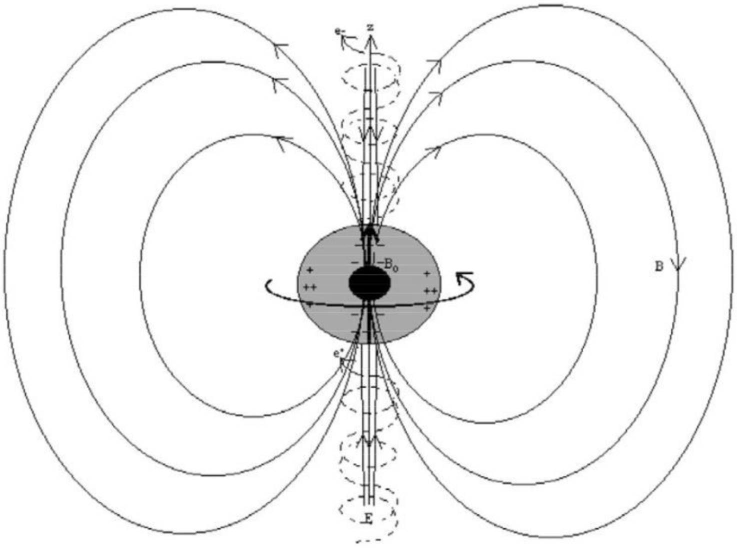

Figure 1.3: The poloidal magnetic field surronding the black hole, and the induced electric field pointing upwards which accelrates the cascade of electron-positron pairs that are produced in the BZ mechanism. Image Credit: Andrea Cattaneo, 2003

The mechanism is based on the solution to Maxwell's equations that shows that the electromagnetic fields themselves carry energy and momentum. According to the model, the black hole at the center of the AGN is threaded by a poloidal magnetic field that is generated by the external currents in the inner accretion disk. This magnetic field extracts the energy from the hole's spin in the form of either Poynting Flux or magnetically driven wind (Livio et al, 1998) that produces the diffuse winds that are observed in some AGN.

In the case where the energy is extracted electromagnetically in the form of Poynting flux, the event horizon of the black hole acts like an electrically conducting surface. Hence, just like a rotating metal sphere inside a magnetic field would generate an electric potential difference, the spinning black hole inside the poloidal field generates a toriodal field at the event horizon that induces an electric potential difference at the surface. This electric potential difference accelerates the ionized plasma at relativistic speeds in opposite directions, perpendicular to plane of the AGN, producing a collimated jet. This model also explains why some radio-quiet AGN have low black hole spins since a black hole with low angular velocity would produce a weaker electric potential difference that can not accelerate the ionized plasma in order to produce a jet.

1.2.2 SUPERLUMINAL MOTION

One of the interesting phenomena that is observed in some radio-loud AGN due to the jet travelling close to the speed of light is the apparent Superluminal motion. The phenomena was first observed in blazar 3C273 where the front blob of the jet was observed to be moving 5 to 10 times the speed of light (Narlikar and Chitre, 1984). This effect simply occurs because the jet is moving towards us at close to the speed of light, and therefore, the two photons emitted by the front blob of the jet reach us in less time than the interval between their emission which makes it look as if the blob covered more distance than it actually did in that interval of time.

1.3 RADIATIVE PROCESSES IN AGN

As shown Fig. 1.1, the AGN consist of different regions and components that emit radiation through different physical processes. These radiative processes can either be thermal and/or non-thermal depending on the region, and therefore, this difference between thermal and non-thermal emissions is mostly used to determine which region has a dominant emission in the spectra of a particular AGN.

1.3.1 ACCRETION DISK EMISSION

Accretion is one of the key processes for generating luminosities in the active galactic nuclei. When a particle from the disk falls on to the black hole, its total energy which is its rotational kinetic energy plus its gravitational potential energy, is dissipated in the form of heat and radiation. This process of converting mechanical energy into radiation can produce very high luminosities depending on the mass accretion rate and the efficiency of converting energy into radiation.The luminosity of such a process is given by Equation 1.1, and the radiation produced in this way gives a blackbody spectrum. However, the entire accretion disk does not have one specific temperature. Instead, the temperature deceases with increasing radius and therefore the inner accretion disk produces high energy photons in UV and soft X-ray bands whereas the emission coming from the outer accretion disk is in the optical and infrared bands.

$$L = \epsilon \dot{M} c^2 \tag{1.1}$$

The ϵ is the efficiency which is equal to R_s/R where R is the radius of the accreting object and R_s is the Schwarzschild radius. Since the efficiency is inversely proportional to the radius of the accreting object, more compact objects have higher efficiency of converting rest mass energy into heat via accretion. A black hole can have an efficiency as high as 0.29. For comparison, the most luminous object in the sky, the

Sun, converts the rest mass energy into heat via fusion with an efficiency of about 0.007 (Rosswog and Bruggen, 2007).

1.3.2 RELATIVISTIC BEAMING AND SYNCHROTRON EMISSION

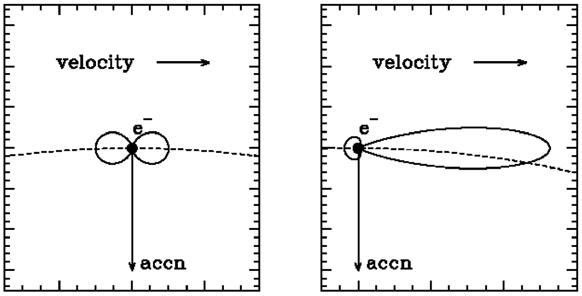

Figure 1.4: An electron travelling at relativistic speed produces a beamed emission in the foward direction if it is accelerated perpendicularly by a magnetic field (right panel) whereas at non-relativtic speed, the emission is not beamed (left panel). Image Credit:http://www.astro.utu.fi/~cflynn/astroII/l4.html

Synchrotron Radiation is one of the dominant, non-thermal radiative processes in AGN. The light produced from synchrotron emission is higly polarized and comes from the relativistic electrons in the jets of AGN. This is because charged particles emit radiation if they are accelerated, and if the charged particle travelling at relativistic speed is accelerated by a magnetic field, then the synchrotron frequency of the emitted radiation is given by Equation 1.2,

$$\omega = \gamma^2 \frac{qB}{mc} \tag{1.2}$$

where γ is the Lorentz factor, q is the charge on the particle, m is the rest mass of the particle, B is the magnetic field strength, and c is the speed of light. Since the charged particle is travelling at relativistic speed, the emission from the accelerated electron is beamed in the forward direction in a cone that has an opening angle of $\frac{1}{\gamma}$. This effect is known as relativistic beaming, and it is this effect that gives blazars and radio-loud quasars their characteristic brightness.

1.3.3 Inverse Compton and Synchrotron-Self Compton

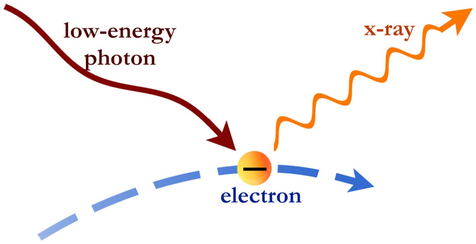

Figure 1.5: The incoming low energy photon is upscattered to high energy photon by colliding with high energy electron. Image Credit:`https://chandra.harvard.edu/resources/illustrations/x-raysLight.html#xlightScatter`

Another process that is common in the spectra of AGN is the Inverse Compton effect. This effect is responsible for producing most of the high-energy photons in AGN as discussed in Section 1.1.1. In this effect, a low-energy photon collides with ultra relativistic electron and gains energy as shown in Fig. 1.5. The amount of energy gained depends on the incident angle and scattering angle of the photon with the ultra-relativistic electron. The maximum energy is gained when the collison between the two occurs head-on. The angle-averaged final energy, E_{final} of the photon is related to E_{initial} by Equation 1.3,

$$E_{\text{final}} = \frac{4\gamma^2 E_{\text{initial}}}{3} \tag{1.3}$$

This effect has a significant contribution in the spectra of jets. The jet produced in AGN travel at relativistic speed and so the electrons in the jet have high energies. The low energy radio photons produced in the jets by ultra-relativistic electrons through synchrotron radiation can collide with the same electrons that produced them. In this way, the radio photons gain energy from the electrons and are boosted to high energy X-ray photons. This process in known as Synchrotron-Self Compton (SSC) and is the dominant process in the X-ray emisson of the jets.

1.3.4 EXTERNAL COMPTON (EC)

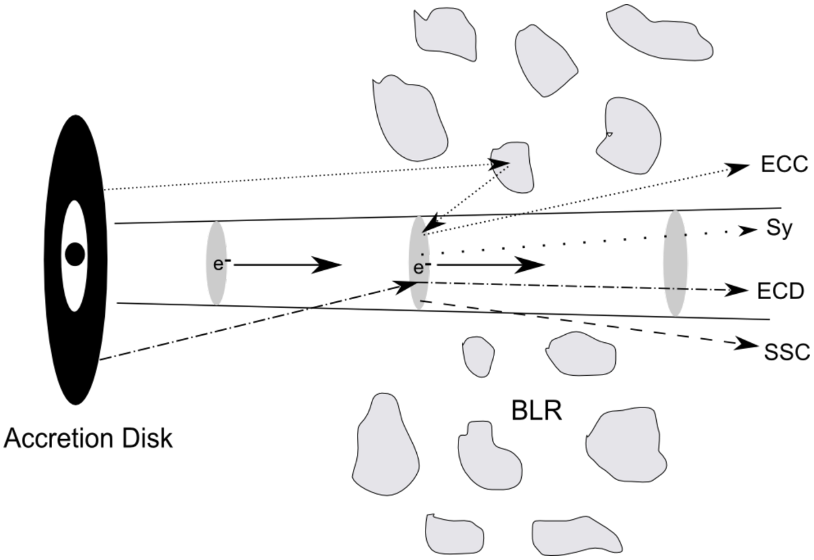

Figure 1.6: The Leptonic Jet Model for blazars where the emission from the accretion disk reprocessed by the BLR and torus(not shown here) that results in External Compton effect. Image credit:`http://large.stanford.edu/courses/2008/ph204/eclov1/`

Apart from the SSC process that takes place in the jet, the inverse Compton effect can also influence the photons that are emitted by the accretion disk as shown in Fig. 1.6. The photons emitted from the accretion disk are reprocessed in the infrared torus and BLR, and are scattered via inverse Compton effect by colliding with the relativistic electrons in the jet. The photons emitted from the disk can also reach the blob of the accelerated electrons in the jet and are therefore scattered directly without being processed by the torus cloud or the BLR. This emission process is known as the External Compton (EC) effect, and is believed to produce the high energy photons in MeV to TeV range of energies.

1.4 XMM-NEWTON SATELLITE

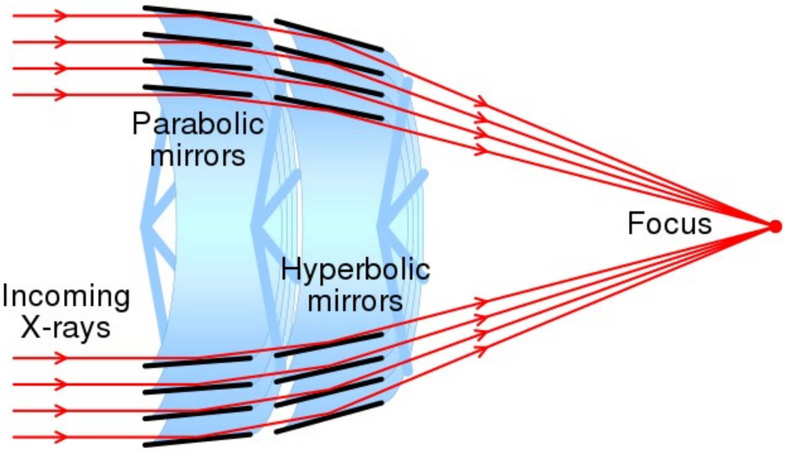

Figure 1.7: TThe XMM newton mirros arrangement. Image credit:`https://www.wikiwand.com/en/X-ray_optics`

The XMM-Newton satellite is a spaced based observatory that observes in the X-ray band from 0.1 keV to 12 keV. The satellite consists of three X-ray telescopes that are based on Wolter I design. The design consist of two types of mirrors which are paraboloid and hyperboloid mirrors. These mirrors reflect the incoming X-ray photons at very small grazing angles towards a focal point as shown in Fig. 1.7. The focal length of the XMM Newton telescope is 7500 mm, and each of the three telescopes has a total of 58 mirrors. The satellite observed blazar 3C273 for a 16 year period from June 2000 to June 2016 through the European Photon Imaging Camera (EPIC). A total of 27 observations of the object were made.

1.5 BLAZAR 3C 273

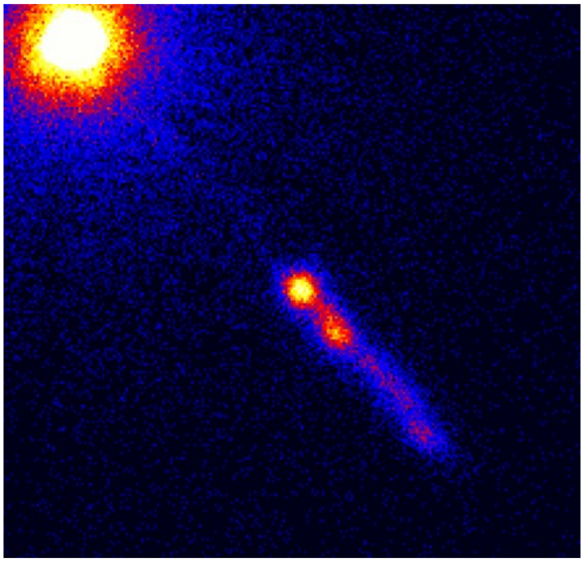

Figure 1.8: The X-ray image of the jet obatined with Chandra X-ray Satellite. Image credit:https://chandra.harvard.edu/photo/2000/0131/index.html

Blazar 3C273 is a radio-loud source with its relativistic jet pointing directly towards Earth. It was discovered in 1963, and it is the nearest quasar to Earth with a redshift of 0.158 (Schmidt, 1963) which makes it an ideal source to study and understand the radio-loud class of AGN. Due to its short distance and extremely high luminosity, 3C273 has been studied in great detail in all wavebands from radio wavelengths to γ-rays, and has shown variability in its flux in all the studied wavebands. Some of its known parameters are:

- $\mathrm{M}_{\mathrm{BH}} = 5 \times 10^{9}\ M_{\odot}$

- $L_{\mathrm{Bol}} = 1.0 \times 10^{47}$ erg s^{-1}
- M_v = -26.8 mag
- Luminosity Distance = 740 Megaparsecs

It is a flat spectrum radio quasar which means its synchrotron emission peaks at lower energies usually in the radio band, and it has a bright excess in the optical-UV band which is known as the Blue Bump (Bhatta et al, 2018). A detailed study of the object in radio band made through the Very long Baseline Interferometry suggests that it has brightness temperature $> 10^{13}$K (Kovalev et al, 2016). The studies that were previously conducted in the X-ray band were based on the same XMM-Newton observations that are used in this work as well. The observations between 2000 to 2003 were studied by Page et al. (2004), that suggested that the soft spectra below 2 keV can be adequately fitted with multiple black body components and the hard band from 2-10 keV can be fitted with a power-law model.

Another X-ray band study done on the observations between 2000-2015 by Kalita et al. (2017), shows that the 2.5-10 keV band is well described by a single power-law, and suggests that the X-ray emission is the result of the Inverse Compton Scattering of the soft UV seed photons emitted from the local environment of the AGN, most likely in a thermal corona.

1.6 THIS THESIS

In this work, we will use the multi-epoch data of 3C 273 to study the spectral variability and examine the nature of the soft excess. Specifically, we will see if the variability in the soft excess is consistent with originating from a black body disc component as suggested by Page et al. (2004).

Chapter 2

Data and Analysis

The multi epoch data for the blazar 3C273 that are used in this work were collected over a period of 16 years from June 2000 to June 2016 with the EPIC-PN instrument on board the XMM-Newton satellite, and the data are shown in Table 2.1. The data were taken from the XMM-Newton Science Archives and all the data processing was done in Gallant et al. (2018). Therefore the data that has been used in this work were processed and also used in that paper. Each of the 27 observations in the data that were made during the 16 year period had different exposure times, and therefore each observation had different quality of data or Signal To Noise Ratio (SNR) as can be seen in Table 2.1 with the highest SNR corresponding to the greatest number of Spectral Data Counts (SDC) in the 0.3-10 keV band. Each observation was given a different spectrum number and it should be noted that given spectrum numbers are not according to the date of the observations with the very first observation corresponding to spectrum number 9.

Since all the data that were used in this work were already processed, the main objectives of this work were to find the simplest mathematical models that would best fit the spectra of 3C273 and then perform analysis on those models to study the long term variability of 3C273 in 2-10 keV and 0.3-10 keV energy bands, and then finally find a physical model that would explain the emission processes that could be taking place in the AGN.

In order to find the model that will best fit the data, different toy-models were fitted to all the 27 observations of the object by using the X-ray Spectral fitting package (Xspec), and the model that gave the best reduced chi-squared values with the least number of parameters or degrees of freedom was selected as the best model for 2-10 keV band and the 0.3-10 keV band.

However, even though different toy-models were tested on each of the 27 observations, the spectra with the highest SNR were of the main focus of study since these spectra had the best quality data, and so if a model was successful in fitting these multi-epoch spectra of 3C273, then it also fitted the rest of the spectra very well. The six spectra with the highest SNR or spectral data counts in the 0.3-10 keV band were spectrum 09, 13, 17, 18, 20, and 27 as can be seen in Table 2.1, and the spectra are shown in Fig. A.1 in the appendix.

Hence for each of the toy models in the following sections, the data obtained after fitting the models to these six spectra are shown in the tables in the section corresponding to the fitted toy model, and the fitted spectra are shown in appendices B and C.

Table 2.1: Data of the blazar 3C273 taken in 0.3-10 keV band with the XMM-Newton satellite from June 2000 to June 2016

Date of Observation	**Observation I.D.**	**Exposure Time (seconds)**	**Spectral Data Counts (0.3-10 keV)**	**Time (Days)**	**Spectrum Number**
06/13/2000	0126700301	73556	1.90672×10^6	0	9
06/15/2000	0126700601	31032	8.43804×10^5	1.554	10
06/15/2000	0126700601	36346	8.28568×10^5	1.994	11
06/17/2000	0126700801	73561	2.73933×10^5	3.989	12
06/13/2001	0136550101	89765	3.33358×10^6	364.315	13
12/16/2001	0112770101	6399	2.26596×10^5	550.663	1
12/22/2001	0112770201	6399	2.17176×10^5	556.028	2
07/07/2002	0112770601	5996	1.68504×10^5	753.615	4
12/17/2002	0112770801	5624	2.44449×10^5	916.948	6
01/05/2003	0136550501	8951	3.38124×10^5	935.609	14
01/05/2003	0112770701	5630	2.0567×10^5	935.739	5
06/18/2003	0112771001	5950	2.75211×10^5	1099.060	7
07/07/2003	0159960101	58557	2.58045×10^6	1118.750	17
07/08/2003	0112770501	8553	3.52902×10^5	1119.453	3
12/14/2003	0112771101	12849	2.84241×10^5	1278.822	8
06/30/2004	0136550801	62913	5.64373×10^5	1477.557	15
07/10/2005	0136551001	28111	8.56839×10^5	1852.591	16
01/12/2007	0414190101	78566	2.66595×10^6	2403.315	18
06/25/2007	0414190301	32511	9.19104×10^5	2567.228	19
12/08/2007	0414190401	35875	2.02243×10^6	2733.855	20
12/09/2008	0414190501	41015	1.62499×10^6	3100.856	21
12/20/2009	0414190601	31912	1.37927×10^6	3476.168	22
12/10/2010	0414190701	36414	1.18695×10^6	3831.081	23
12/12/2011	0414190801	43915	1.29094×10^6	4198.753	24
07/16/2012	0414191001	38918	6.53562×10^5	4415.513	25
07/13/2015	0414191101	72400	1.57988×10^6	5507.892	26
06/26/2016	0414191201	67200	2.56082×10^6	5856.863	27

Chapter 3

MODELLING 2-10 keV

The hard X-ray band of 3C273 was first studied with two different mathematical models which were single power-law and broken power-law, and the model that best described all the 27 spectra was examined further to study the variability of 3C273 in the hard x-ray band. The spectral parameters of the best fit model were also examined to study their variability with time and for any correlations that would explain any physical process taking place around the AGN.

3.1 FITTING SINGLE POWER-LAW

As discussed in Sect. 1.3, the emission from AGN can either be thermal and/or non-thermal depending on its particular regions. This non-thermal emission coming from a single electron or a charged particle produces a spectrum that has a sharp peak at a specific frequency as shown in the upper panel of Fig. 3.1.

However, since in AGN we have electrons with a broad energy distribution where each electron is at a different energy, the emission spectrum produced by a distribition of electrons undergoing a non-thermal emission process such as synchrotron or inverse Compton is a series of these peaks each at a different frequency as shown in the lower panel of Fig. 3.1. The resulting spectrum is a power-law shape on a logarithmic scale as shown in Fig. 3.2a with a negative slope Γ and a normlaization constant, K which

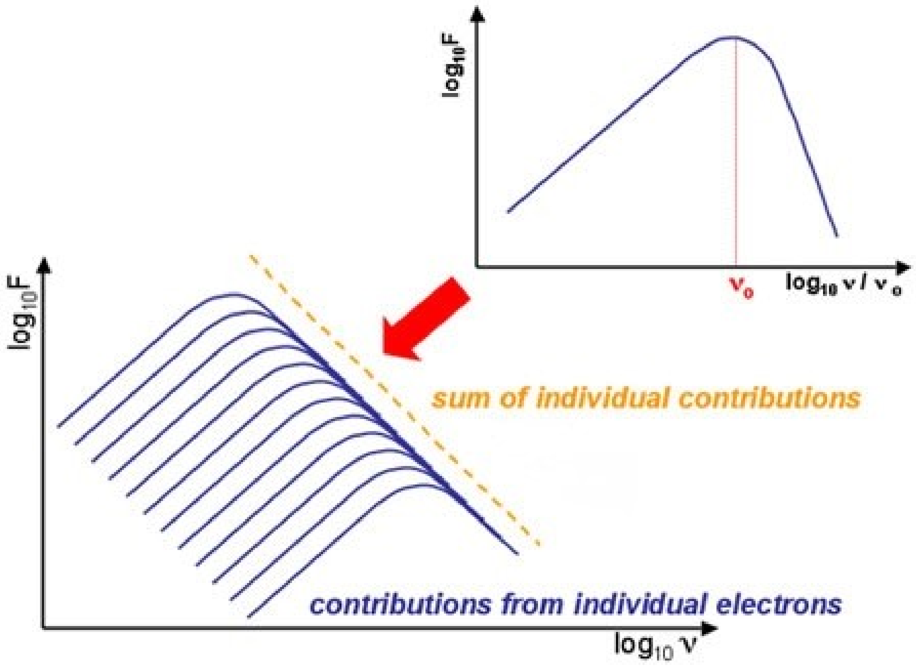

Figure 3.1: Non-Thermal Emission spectrum resulting from an electron distrbution undergoing synchrotron and/or inverse Compton effect around the AGN. Image credit:`http://astronomy.swin.edu.au/cosmos/S/Synchrotron+Emission`

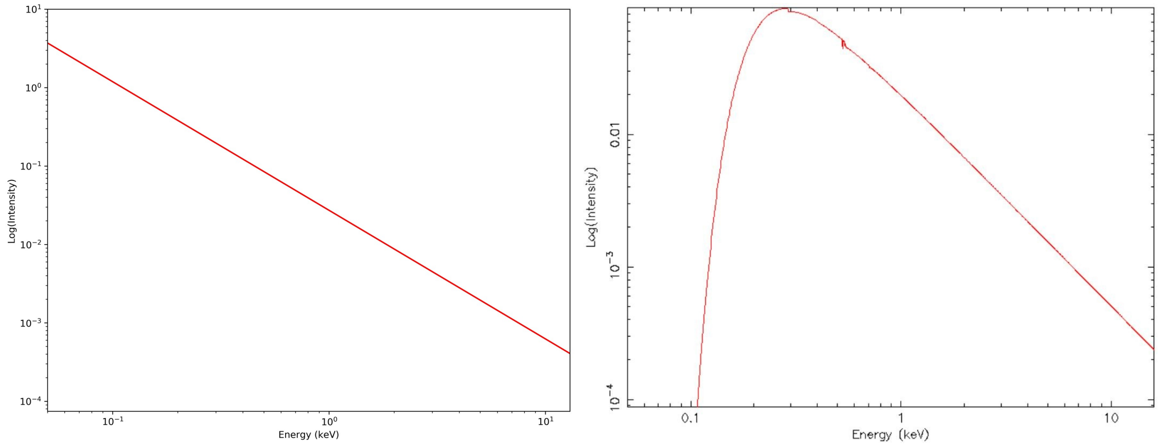

(a)

(b)

Figure 3.2: The (a) unabsorbed single power-law, and (b) the redshifted, absorbed single power-law that was used to study the non-thermal emission of 3C273 in the hard X-ray band

determines the flux at 1 keV as shown in Equation 3.1.

$$I(E) = KE^{-\Gamma} \tag{3.1}$$

Hence in order to study the hard band of 3C273, a redshifted single, asborbed power-law shown in Fig. 3.2b was fitted to 2-10 keV band. The redshifted, absobed power-law was chosen to account for the Galactic absorption and redhsift of 3C273 which are equal to 1.77×10^{20} atoms cm^{-2} (UK Swift Data Science Center, 2013) and 0.158 respectively.

3.1.1 RESULTS AND ANALYSIS

The single power-law model fitted to all the 27 spectra of 3C273 gave an average reduced χ^2 value of 1.07, and therefore it defined the spectra of 3C273 relatively well. However, as can be seen from the fits of the six spectra with the highest SNR in Fig B.2, the high energy near 10 keV and low energy near 2 keV lie above the $\frac{data}{model}$ ratio line in the lower panels of Fig. B.2 where the data for fits is shown in Table 3.1.

Although this hints at a possible emission feature around these two ends, the low energy end around 2 keV fitted quite well once the broadband spectrum (0.3-10 keV) was analysed with different, more complex models and so it suggests that it is just the data near 2 keV that does not fit very well with a single power-law.

The fitting of the high-energy near 10 keV was however more complicated than 2 keV. This is because even with more complex models in the analysis of the broadband, not all the models were able to fit the high energy end.

Table 3.1: Single Power-Law Data

Spectrum Number	**Reduced χ^2**	**Γ**	**Normalization** $(photonskeV^{-2}cm^{-2}s^{-1})$ 10^{-2}	**Flux (2-10 keV)** $(ergcm^{-2}s^{-1})$ 10^{-11}
09	1.02	1.627 ± 0.006	2.25 ± 0.02	8.10 ± 0.02
13	1.18	1.608 ± 0.005	2.60 ± 0.02	9.68 ± 0.02
17	1.22	1.784 ± 0.006	3.55 ± 0.03	9.78 ± 0.01
18	1.25	1.392 ± 0.005	2.38 ± 0.02	12.91 ± 0.02
20	1.05	1.598 ± 0.006	4.22 ± 0.04	15.99 ± 0.03
27	1.27	1.478 ± 0.005	2.73 ± 0.02	12.72 ± 0.02

Apart from the fits of the spectra, the spectral parameters of the single power-law model were analysed including the model flux of the object in the 2-10 keV band, and it was found that the object was brightest in 2007 as shown in Fig. 3.3, and the dimmest in 2015. Although not a particular trend was observed in the hard band flux, the variability seen in the flux is what is typically observed in AGN. Other than the flux, the slope, Γ, of the single power law was plotted against time in Fig. 3.4 to examine the trend which shows a slight decrease in the slope of the single power-law over the years.

The slope was also plotted against the normalization to investigate any possible correlation which could hint at a softer-when-brighter or harder-when-brighter trend in the hard band. Although a weak positve trend was observed, the correlation coefficient between the two parameters of the model was calculated to be less than 0.5, and therefore, the correlation was not investigated in detail.

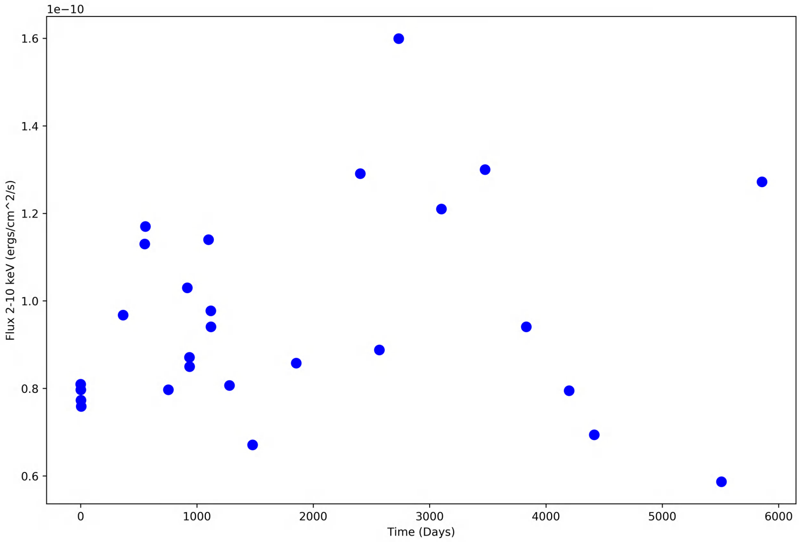

Figure 3.3: Hard band flux of 3C273 observed from June 2000 to June 2016. Error bars are present but are smaller than the data points.

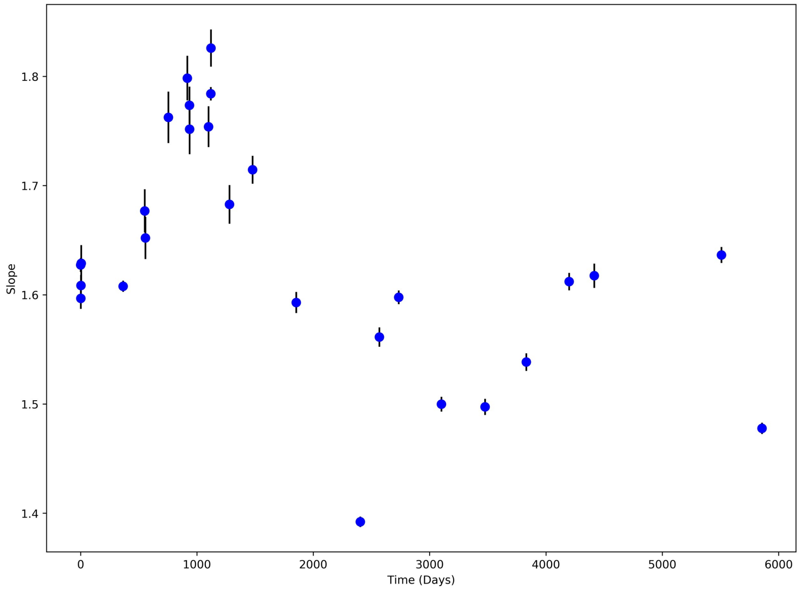

Figure 3.4: The change in the slope of the single power-law over the period of 16 years.

3.1.2 VARIABILITY OF SPECTRAL PARAMETERS

The variability of the spectral parameters of the single power-law model was analysed as shown in Fig. 3.5. The fractional variability of the parameters was calculated using Equation 3.2 and the error on the fractional variability was calculated by using

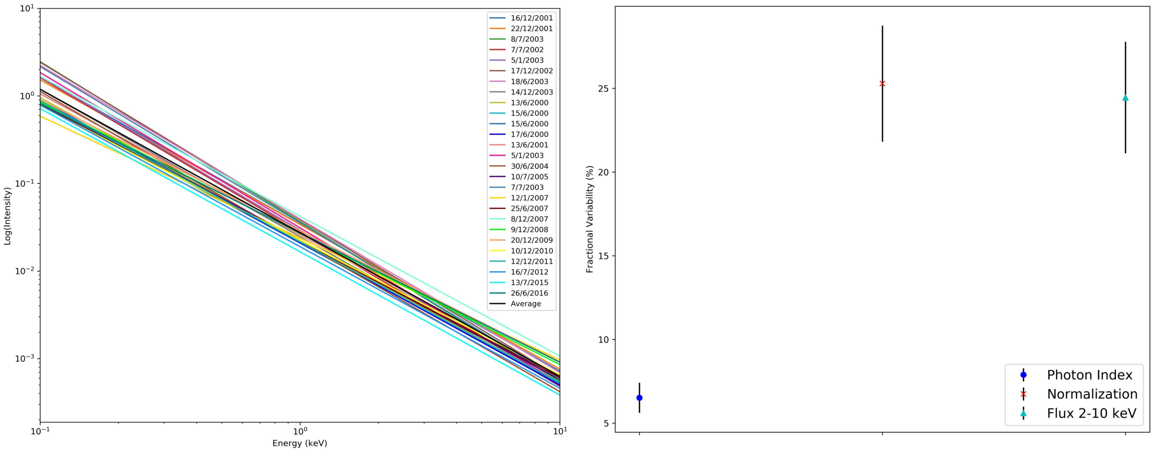

Figure 3.5: The variability of the single power law model of 3C273 over a period of 16 years.

Equation 3.3 (Edelson et al, 2001).

$$F_{Var} = \sqrt{\frac{S^2 - \langle \sigma_{err}^2 \rangle}{\langle X \rangle^2}} \tag{3.2}$$

$$\sigma_{F_{Var.}} = \frac{1}{F_{var.}} \sqrt{\frac{1}{2N}} \frac{S^2}{\langle X \rangle^2} \tag{3.3}$$

where S^2 is the variance of the parameter, $\langle \sigma_{err}^2 \rangle$ is the average error squared on the values of the parameter, $\langle X \rangle^2$ is the square of the average value of the parameter, and N is the number of data points.

As shown in the figure above, the most variable parameter was the normalization of the single power-laws fitted to the 27 spectra while the shape of the power-laws did not vary much since the slope had the smallest fractional variability of about 6%. Hence this suggests that the shape of the spectrum of 3C273 stays approximately the same while the height of the spectrum vary over time but not with a specific trend.

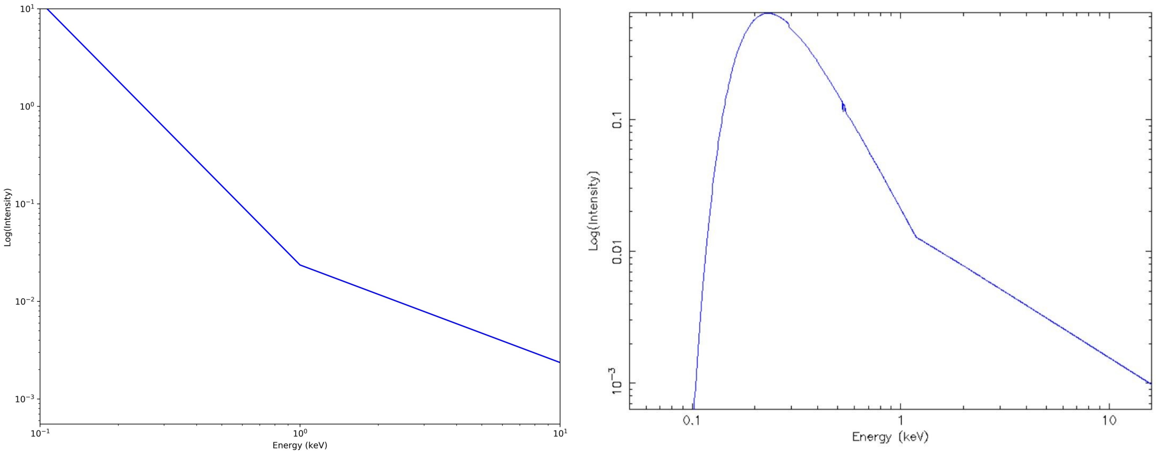

(a)

(b)

Figure 3.6: The broken power-laws used to study the hard band of 3C273 where a) is the unabsorbed model, and b) is the absorbed power-law with $N_H = 1.77 \times 10^{20}$ atoms cm^{-2} that was fitted to the 26 spectra.

3.2 FITTING BROKEN POWER-LAW

Although the 2-10 keV band was succesfully fitted with a single power-law model with the highest reduced χ^2 value of 1.3 corresponding to spectrum 27 in Table 3.1, a broken power-law model was also tested to see if the model could show any significant result when fitted to data. As shown in Fig. 3.6, the broken power law model has two slopes, Γ_1 and Γ_2, a break energy where the value of the slope changes from Γ_1 to Γ_2, and a normalization constant, K. Therefore, this model was tested to see if there could be a non-thermal emission process taking place in the AGN in the 2-10 keV band where the slope changes from Γ_1 to Γ_2, or it could be that two different regions in the AGN could both be emitting radiation via non-thermal emission process resulting in two different slopes.

Table 3.2: Broken Power-Law Data for 2-10 keV

Spectrum Number	**Reduced** χ^2	Γ_1	**Break Energy (keV)**	Γ_2	**Normalization** $(photons keV^{-2}$ $cm^{-2} s^{-1})$ 10^{-2}	**Flux** $(erg cm^{-2} s^{-1})$ 10^{-11}
09	1.01	$1.66^{+0.02}_{-0.02}$	$4.4^{+0.8}_{-0.7}$	$1.60^{+0.01}_{-0.02}$	$2.33^{+0.05}_{-0.05}$	$8.12^{+0.02}_{-0.01}$
13	1.08	$1.70^{+0.02}_{-0.02}$	$4.2^{+0.3}_{-0.3}$	$1.54^{+0.01}_{-0.01}$	$2.87^{+0.06}_{-0.06}$	$9.73^{+0.01}_{-0.02}$
17	1.12	$1.87^{+0.02}_{-0.02}$	$4.5^{+0.3}_{-0.3}$	$1.69^{+0.02}_{-0.02}$	$3.92^{+0.08}_{-0.08}$	$9.84^{+0.02}_{-0.02}$
18	1.11	$1.44^{+0.01}_{-0.01}$	$6.3^{+0.4}_{-0.5}$	$1.23^{+0.04}_{-0.03}$	$2.51^{+0.03}_{-0.03}$	$13.03^{+0.02}_{-0.02}$
20	0.97	$1.64^{+0.01}_{-0.01}$	$6.00^{+0.03}_{-0.04}$	$1.45^{+0.03}_{-0.03}$	$4.46^{+0.06}_{-0.06}$	$16.13^{+0.04}_{-0.03}$
27	1.10	$1.55^{+0.01}_{-0.01}$	$5.2^{+0.3}_{-0.2}$	$1.35^{+0.02}_{-0.02}$	$2.99^{+0.04}_{-0.04}$	$12.84^{+0.02}_{-0.02}$

3.2.1 Results

As shown in Table 3.2, and Fig. B.1, the model sucessfully fits the six best quality spectra with the highest reduced χ^2 value being 1.1. Although the high energy near 10 keV is still not fitted well as shown in the lower panel of the fits in Fig. B.1. However, one of the reason the fits were better than the single power-law was because it had two extra parameters which were break energy and Γ_2. Apart from that, the model does not define the hard band well enough because it could not fit spectrum 12 at all, and while fitting the model to different spectra in Xspec, the error was given which suggested that the break energy parameter was insensitive to the fit. Hence this suggested that the model was too complicated given the data quality, and so the single power-law model was taken as the best fit model for the hard band of 3C273.

Chapter 4

MODELLING 0.3-10 keV

The analysis on the broadband (0.3-10 keV) were performed in a similar way where a total of four toy models were tested on each of the 27 spectra of 3C273. Each model accounted for different physical processes that could be taking place in the AGN which would result in thermal and/or non-thermal emission. The goal was to find the simplest model with the least number of parameters that would give the lowest χ^2 values for the fits. Once the best fit model was found, the analysis were performed on its spectral parameters to examine their variability with time and also to find any correlations between the parameters that would suggest any physical processes taking place in the AGN.

4.1 BROKEN POWER-LAW

The broken power-law model was fitted to the broad 0.3-10 keV band since the broadband has a higher probability of exhibiting non-thermal processes where the emission could be arising from different regions of the AGN with different power-law slopes. The absorbed power-law as shown in Fig. 3.6 was fitted to all the 27 spectra. However, the presence of the Galactic absoption was much more significant in broadband than 2-10 keV band since the broadband involved lower energy range.

Table 4.1: Broken Power-Law Data

Spectrum Number	**Reduced χ^2**	$\mathbf{\Gamma_1}$	**Break Energy (keV)**	$\mathbf{\Gamma_2}$	**Normalization ($photonskeV^{-2}$ $cm^{-2}s^{-1}$) 10^{-2}**
09	1.43	2.044 ± 0.007	1.34 ± 0.03	1.670 ± 0.004	2.683 ± 0.008
13	2.16	2.227 ± 0.006	1.37 ± 0.03	1.669 ± 0.003	3.415 ± 0.008
17	1.34	2.068 ± 0.005	1.41 ± 0.04	1.814 ± 0.004	4.058 ± 0.009
18	1.90	1.899 ± 0.007	1.31 ± 0.02	1.442 ± 0.003	2.913 ± 0.008
20	1.45	2.084 ± 0.007	1.30 ± 0.02	1.644 ± 0.004	5.09 ± 0.02
27	1.55	1.887 ± 0.005	1.42 ± 0.02	1.513 ± 0.004	3.290 ± 0.007

Table 4.2: Broken Power-Law flux where all the flux values are in units of ergcm^{-2}s^{-1}

Spectrum Number	**Soft Band Flux(0.3-2 keV)** 10^{-11}	**Hard Band Flux (2-10 keV)** 10^{-11}	**Flux (0.3-10 keV)** 10^{-11}	**Hardness Ratio** $\left(\frac{\mathrm{SoftBand}}{\mathrm{HardBand}}\right)$
09	$5.643^{+0.004}_{-0.003}$	$8.04^{+0.01}_{-0.01}$	$13.69^{+0.02}_{-0.02}$	$0.702^{+0.001}_{-0.001}$
13	$7.357^{+0.005}_{-0.006}$	$9.59^{+0.02}_{-0.02}$	$16.94^{+0.02}_{-0.02}$	$0.768^{+0.002}_{-0.002}$
17	$8.418^{+0.006}_{-0.007}$	$9.74^{+0.01}_{-0.02}$	$18.16^{+0.03}_{-0.03}$	$0.864^{+0.001}_{-0.002}$
18	$6.185^{+0.005}_{-0.004}$	$12.81^{+0.02}_{-0.02}$	$18.99^{+0.02}_{-0.02}$	$0.4830^{+0.0007}_{-0.0006}$
20	$10.84^{+0.01}_{-0.01}$	$15.86^{+0.04}_{-0.03}$	$26.71^{+0.03}_{-0.03}$	$0.684^{+0.002}_{-0.002}$
27	$6.846^{+0.004}_{-0.006}$	$12.66^{+0.02}_{-0.02}$	$19.50^{+0.03}_{-0.01}$	$0.5408^{+0.0001}_{-0.0009}$

4.1.1 Results

Tables 4.1 and 4.2 show the data for the fits of the six spectra which had the highest SNR, and the fits of spectra are shown in Fig. C.1. As shown in Table 4.1, the highest reduced χ^2 value for the fit is 2.1 corresponding to spectrum 13, and this suggests that the model is not a good fit for the data. Also the data points near the high energy in Fig. C.1 lie significantly above the ratio line in the lower panels of the figures. Hence a broken power-law with two different slopes does not describe the spectrum very well.

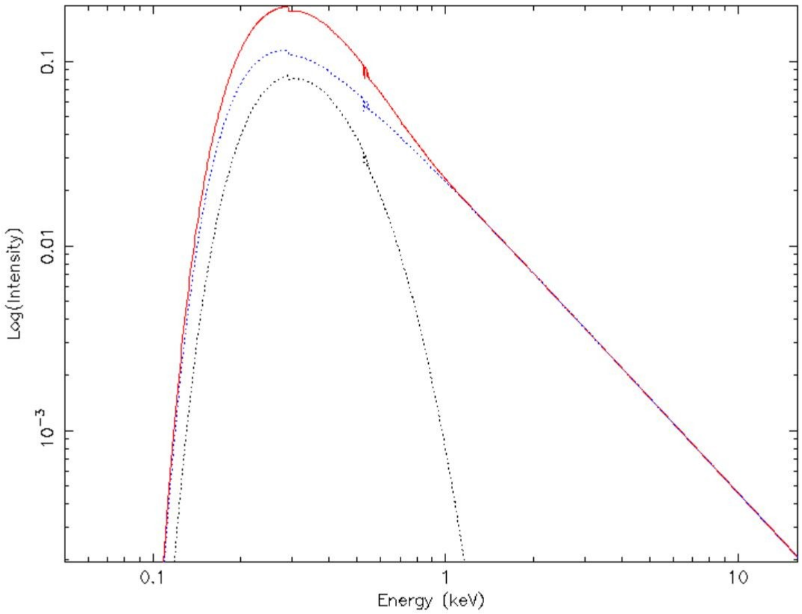

Figure 4.1: The absorbed blackbody plus power law model where the black dotted line shows the thermal component, the blue line shows the non-thermal component, and the red line is the combined model

4.2 POWER-LAW+BLACKBODY

Since the broken power-law accounted for only the non-thermal emission coming from different regions of the AGN which was unable to fit the 0.3-10 keV band, the blackbody plus power law model in Fig. 4.1, was tested. This is because the emission arising from the accretion disk is thermal (Sect. 1.3.1), and therefore, if the spectrum of 3C273 includes both, a thermal and a non-thermal component, then this model should be able to fit the data.

4.2.1 Results

The results from the model fits are shown in Tables 4.3 and 4.4, and the fits are shown in Fig. C.2. As shown in the fits in Fig. C.2, the model is clearly unable to fit the

Table 4.3: Power-law+BlackBody Data

.

Spectrum Number	**Reduced χ^2**	**Photon Index, Γ**	**Norm$_{pw}$ ($photonskeV^{-2}$ $cm^{-2}s^{-1}$) 10^{-2}**	**Temperature (keV)** 10^{-1}	**Norm$_{bb}$ ($ergs^{-1}kpc^{-2}$)** 10^{-4}
09	1.49	$1.692^{+0.003}_{-0.003}$	$2.477^{+0.009}_{-0.009}$	$1.07^{+0.01}_{-0.01}$	$2.29^{+0.04}_{-0.04}$
13	2.64	$1.703^{+0.003}_{-0.003}$	$2.99^{+0.01}_{-0.01}$	$1.09^{+0.01}_{-0.01}$	$4.56^{+0.06}_{-0.06}$
17	1.42	$1.828^{+0.003}_{-0.003}$	$3.79^{+0.01}_{-0.01}$	$1.15^{+0.02}_{-0.01}$	$2.48^{+0.05}_{-0.05}$
18	1.97	$1.459^{+0.003}_{-0.003}$	$2.638^{+0.008}_{-0.008}$	$1.12^{+0.01}_{-0.01}$	$2.61^{+0.03}_{-0.03}$
20	1.55	$1.661^{+0.003}_{-0.003}$	$4.64^{+0.02}_{-0.02}$	$1.09^{+0.01}_{-0.01}$	$5.01^{+0.07}_{-0.07}$
27	1.75	$1.534^{+0.003}_{-0.003}$	$2.971^{+0.009}_{-0.009}$	$1.17^{+0.01}_{-0.01}$	$2.49^{+0.03}_{-0.03}$

Table 4.4: Power-law+Blackbody flux where all the flux values are in units of erg cm^{-2} s^{-1}

Spectrum Number	**Soft Band Flux(0.3-2 keV)** 10^{-11}	**Hard Band Flux (2-10 keV)** 10^{-11}	**Flux (0.3-10 keV)** 10^{-11}	**Hardness Ratio** $\left(\frac{\text{SoftBand}}{\text{HardBand}}\right)$
09	$5.649^{+0.005}_{-0.005}$	$7.971^{+0.01}_{-0.01}$	$13.62^{+0.01}_{-0.02}$	$0.7089^{+0.001}_{-0.001}$
13	$7.349^{+0.005}_{-0.005}$	$9.45^{+0.02}_{-0.02}$	$16.80^{+0.02}_{-0.02}$	$0.778^{+0.001}_{-0.001}$
17	$8.404^{+0.006}_{-0.007}$	$9.68^{+0.02}_{-0.01}$	$18.08^{+0.02}_{-0.02}$	$0.868^{+0.002}_{-0.001}$
18	$6.190^{+0.001}_{-0.004}$	$12.72^{+0.02}_{-0.02}$	$18.91^{+0.01}_{-0.02}$	$0.4867^{+0.0009}_{-0.0008}$
20	$10.834^{+0.006}_{-0.004}$	$15.75^{+0.02}_{-0.03}$	$26.58^{+0.04}_{-0.03}$	$0.688^{+0.001}_{-0.001}$
27	$6.845^{+0.004}_{-0.005}$	$12.56^{+0.02}_{-0.03}$	$19.40^{+0.02}_{-0.02}$	$0.545^{+0.001}_{-0.001}$

data with most of the data points near 10 keV being significantly above the ratio line and the highest reduced χ^2 value being 2.6 that corresponds to spectrum 13. This suggests that the spectrum of 3C273 most probably does not have a thermal origin and therefore could not be originating in the accretion disk.

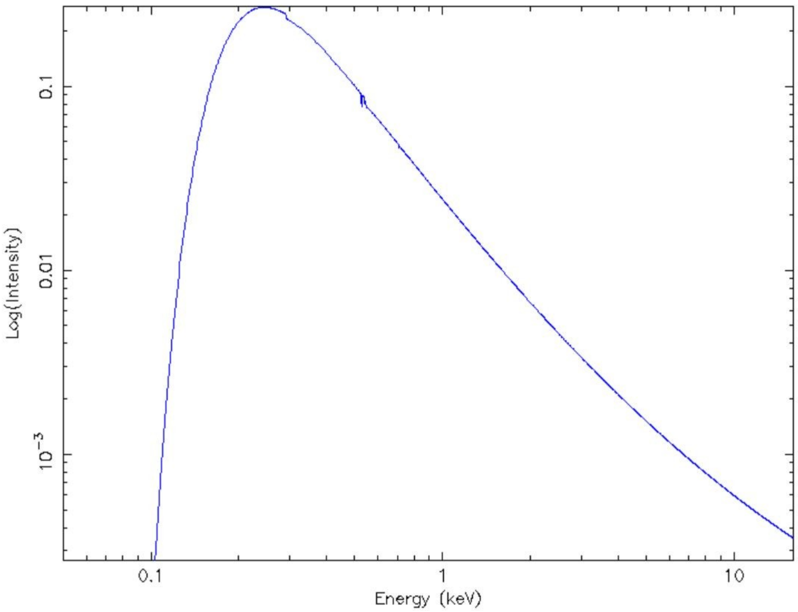

Figure 4.2: The absorbed log-parabola model

4.3 LOG-PARABOLA MODEL

The next model that was tested was the log parabola model for bazars shown in Fig. 4.2. Unlike the previous models, the slope of this model is not fixed but changes gradually with energy, E as shown in Fig. 4.2. Therefore, if the spectrum of 3C273 has a slope that changes with energy, then this model should be able to give better fits than the previous two models. The model has a total of three parameters as shown in Equation 4.1

$$I(E) = K\left(\frac{E}{E_{pivot}}\right)^{-a-b\log\frac{E}{E_{pivot}}} \tag{4.1}$$

where a is the slope at the pivot energy, b determines the curvature of parabola, and K is the normalization constant. The pivot energy, E_{pivot} is not a parameter but a constant.

Table 4.5: Log-parabola Data

Spectrum Number	**Reduced** χ^2	**Pivot Energy (keV)**	**Photon Index,** α	**Curvature Term, b**	**Normalization** $(photonskeV^{-1}$ $cm^{-2}s^{-1})$ 10^{-2}
09	1.34	0.8	$1.998^{+0.003}_{-0.003}$	$-0.271^{+0.004}_{-0.004}$	$4.203^{+0.006}_{-0.006}$
13	1.75	0.8	$2.169^{+0.002}_{-0.002}$	$-0.409^{+0.003}_{-0.003}$	$5.541^{+0.006}_{-0.006}$
17	1.25	0.8	$2.048^{+0.003}_{-0.003}$	$-0.192^{+0.004}_{-0.004}$	$6.388^{+0.008}_{-0.008}$
18	1.67	0.8	$1.829^{+0.003}_{-0.003}$	$-0.317^{+0.004}_{-0.003}$	$4.424^{+0.006}_{-0.006}$
20	1.37	0.8	$2.020^{+0.003}_{-0.003}$	$-0.314^{+0.004}_{-0.004}$	$8.06^{+0.01}_{-0.01}$
27	1.32	0.8	$1.855^{+0.003}_{-0.003}$	$-0.273^{+0.004}_{-0.004}$	$4.961^{+0.006}_{-0.006}$

Table 4.6: Log-parabola flux where all the flux values are in units of erg cm^{-2} s^{-1}

Spectrum Number	**Soft Band Flux(0.3-2 keV)** 10^{-11}	**Hard Band Flux (2-10 keV)** 10^{-11}	**Flux (0.3-10 keV)** 10^{-11}	**Hardness Ratio** $\left(\frac{\text{SoftBand}}{\text{HardBand}}\right)$
09	$5.668^{+0.006}_{-0.004}$	$8.19^{+0.02}_{-0.01}$	$13.86^{+0.01}_{-0.01}$	$0.692^{+0.002}_{-0.001}$
13	$7.416^{+0.007}_{-0.005}$	$9.85^{+0.02}_{-0.01}$	$17.27^{+0.01}_{-0.02}$	$0.753^{+0.001}_{-0.002}$
17	$8.448^{+0.006}_{-0.005}$	$9.86^{+0.02}_{-0.02}$	$18.31^{+0.01}_{-0.02}$	$0.857^{+0.002}_{-0.002}$
18	$6.218^{+0.004}_{-0.005}$	$13.12^{+0.02}_{-0.02}$	$19.34^{+0.02}_{-0.02}$	$0.4737^{+0.0007}_{-0.0009}$
20	$10.89^{+0.01}_{-0.01}$	$16.25^{+0.04}_{-0.04}$	$27.14^{+0.02}_{-0.04}$	$0.670^{+0.002}_{-0.002}$
27	$6.888^{+0.004}_{-0.005}$	$12.89^{+0.03}_{-0.01}$	$19.78^{+0.02}_{-0.02}$	$0.534^{+0.001}_{-0.001}$

4.3.1 Results

The results for the log parabola modelling are shown in Tables 4.5 and 4.6, and the fits are shown in Fig. C.3. The model was able to fit the data better than the previous two models since the highest reduced χ^2 value for the fit of spectrum 13 was 1.75. Therefore, this suggests that the spectrum of 3C273 may not have one or two distinct slopes but instead, it may be parabolic in nature or has a slope that changes gradually with increasing energy. However, even though the fits got better with this model, the model still does not fit the high energy end well enough as shown in the lower panels of Fig. C.3 where the data points are significantly below the ratio line. Hence, this model was considered better than the previous two models since it had one less parameter than the other two and gave better fits, but it was still not the best fit model

4.4 DOUBLE POWER-LAW MODEL

The double power-law model was the next model that was tested to fit the data of 3C273. The equation for the model is,

$$I(E) = K_{Hard}E^{-\Gamma_{Hard}} + K_{Soft}E^{-\Gamma_{Soft}} \tag{4.2}$$

where K_{Hard} is the normalization of the power law that is dominant in the hard band in Fig. 4.3b, Γ_{Hard} is the slope of the power-law that is dominant in the hard band and similarly, K_{Soft} and Γ_{Soft} correspond to the normalization and slope respectively, of the power law that is dominant in the soft band in Fig. 4.3b. Also, Fig. 4.3 shows the plot of Equation 4.2 on logarithmic scales. The slope of the double power-law model, as shown in Fig. 4.3 changes in a similar way to the log-parabola model, but has a greater curvature at its center while the two ends are approximately straight lines. Therefore, unlike broken power-law, the slope of the of model does not change at a single energy value, but changes gradually from Γ_{soft} to Γ_{Hard}. Thus, it accounts for the non-thermal emission processes that could be changing their slope in this way

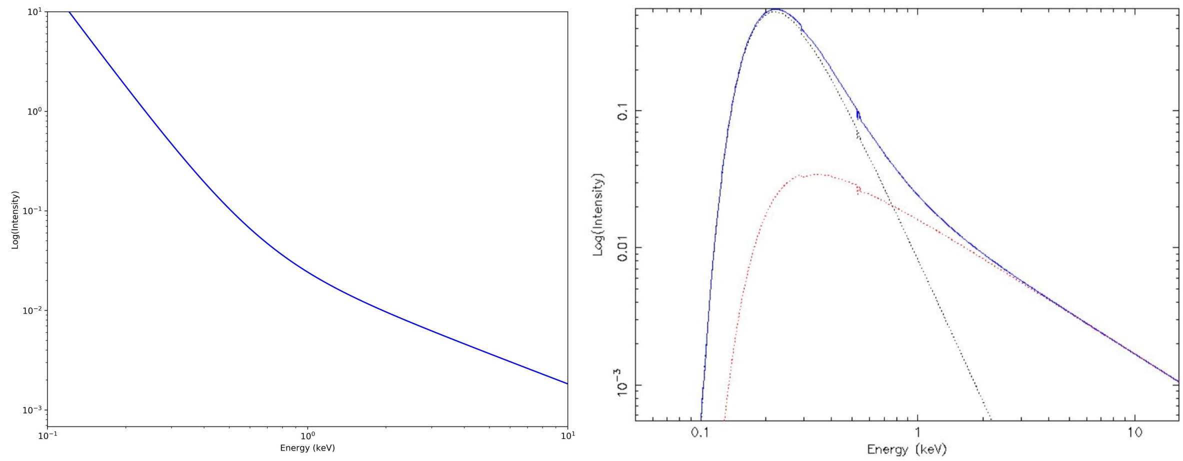

(a) (b)

Figure 4.3: The double power-law models on logarithmic scales where a) is the unabsorbed power-law and b) is the absorbed, redshifted power-law

and so this model was fitted to all the 27 spectra.

4.4.1 Results and Analysis

The result of the fits are shown in Tables 4.7 and 4.8, and the fits for the six spectra with the highest SNR are shown in Fig. C.4. As can be seen from the fits, the model was able to fit the entire broadband range (0.3-10 keV) of the data including the high energy near 10 keV for most of the spectra. The highest reduced χ^2 value calculated was 1.2 corresponding to spectra 13, 17, 18, and 27. Therefore, the double power-law described the spectrum of 3C273 with significant success and so different analysis were performed on its parameters to find any trends and correlations that woud hint at any physical processes taking place in the AGN. Also, since the double power-law involves two power laws fitting the spectrum of 3C273, the total flux calculated by the model is the sum of the flux coming from the hard power-law and the soft power-law. Therefore, the flux coming from the soft power-law, F_{Γ_s}, was also calculated for all the 27 spectra, and is shown in Table 4.8 for the six spectra for reference.

Table 4.7: Double Power-Law Data

Spectrum Number	**Reduced** χ^2	$\Gamma_{\mathbf{Hard}}$	**Norm**$_{\mathbf{Hard}}$ $(\boldsymbol{photonskeV^{-1} cm^{-2}s^{-1}})$ 10^{-2}	$\Gamma_{\mathbf{Soft}}$	**Norm**$_{\mathbf{Soft}}$ $(\boldsymbol{photonskeV^{-1} cm^{-2}s^{-1}})$ 10^{-2}
09	1.12	$1.55^{+0.01}_{-0.01}$	$1.87^{+0.05}_{-0.06}$	$2.85^{+0.06}_{-0.05}$	$0.792^{+0.06}_{-0.06}$
13	1.20	$1.48^{+0.01}_{-0.01}$	$1.95^{+0.04}_{-0.04}$	$2.91^{+0.03}_{-0.03}$	$1.44^{+0.04}_{-0.04}$
17	1.23	$1.60^{+0.03}_{-0.03}$	$2.2^{+0.2}_{-0.2}$	$2.48^{+0.05}_{-0.05}$	$1.9^{+0.2}_{-0.2}$
18	1.20	$1.32^{+0.01}_{-0.01}$	$2.01^{+0.04}_{-0.04}$	$2.76^{+0.04}_{-0.04}$	$0.89^{+0.04}_{-0.04}$
20	1.10	$1.50^{+0.01}_{-0.01}$	$3.4^{+0.1}_{-0.1}$	$2.85^{+0.05}_{-0.05}$	$1.7^{+0.1}_{-0.1}$
27	1.18	$1.35^{+0.01}_{-0.02}$	$2.00^{+0.07}_{-0.07}$	$2.52^{+0.04}_{-0.04}$	$1.26^{+0.08}_{-0.07}$

Table 4.8: Double Power-Law flux table where all flux values are in units of erg cm^{-2} s^{-1}

Spectrum Number	**Soft Band Flux(0.3-0.8 keV)** 10^{-11}	**Hard Band Flux (2-10 keV)** 10^{-11}	**Flux (0.3-10 keV)** 10^{-11}	**Hardness Ratio** $\left(\frac{\text{Softband}}{\text{HardBand}}\right)$	F_{Γ_S} 10^{-11}	$\frac{F_{\Gamma_S}}{F_{Total}}$
09	$2.676^{+0.003}_{-0.004}$	$8.12^{+0.01}_{-0.02}$	$13.80^{+0.02}_{-0.02}$	$0.3296^{+0.0007}_{-0.0009}$	$2.270^{+0.003}_{-0.004}$	$0.1644^{+0.0003}_{-0.0004}$
13	$3.774^{+0.004}_{-0.004}$	$9.73^{+0.01}_{-0.02}$	$17.17^{+0.01}_{-0.02}$	$0.3878^{+0.0007}_{-0.0008}$	$4.126^{+0.003}_{-0.004}$	$0.2404^{+0.0003}_{-0.0003}$
17	$4.075^{+0.004}_{-0.007}$	$9.83^{+0.02}_{-0.02}$	$18.28^{+0.02}_{-0.02}$	$0.414^{+0.001}_{-0.001}$	$5.707^{+0.006}_{-0.007}$	$0.31220^{+0.0005}_{-0.0005}$
18	$2.691^{+0.003}_{-0.003}$	$12.96^{+0.02}_{-0.02}$	$19.20^{+0.02}_{-0.02}$	$0.2076^{+0.0004}_{-0.0005}$	$2.559^{+0.003}_{-0.003}$	$0.1333^{+0.0002}_{-0.0002}$
20	$5.187^{+0.006}_{-0.008}$	$16.61^{+0.03}_{-0.03}$	$26.99^{+0.03}_{-0.02}$	$0.3228^{+0.0008}_{-0.0007}$	$4.852^{+0.005}_{-0.004}$	$0.1797^{+0.0003}_{-0.0002}$
27	$3.008^{+0.003}_{-0.004}$	$12.79^{+0.03}_{-0.01}$	$19.69^{+0.01}_{-0.03}$	$0.2351^{+0.0005}_{-0.0004}$	$3.800^{+0.003}_{-0.005}$	$0.1930^{+0.0002}_{-0.0004}$

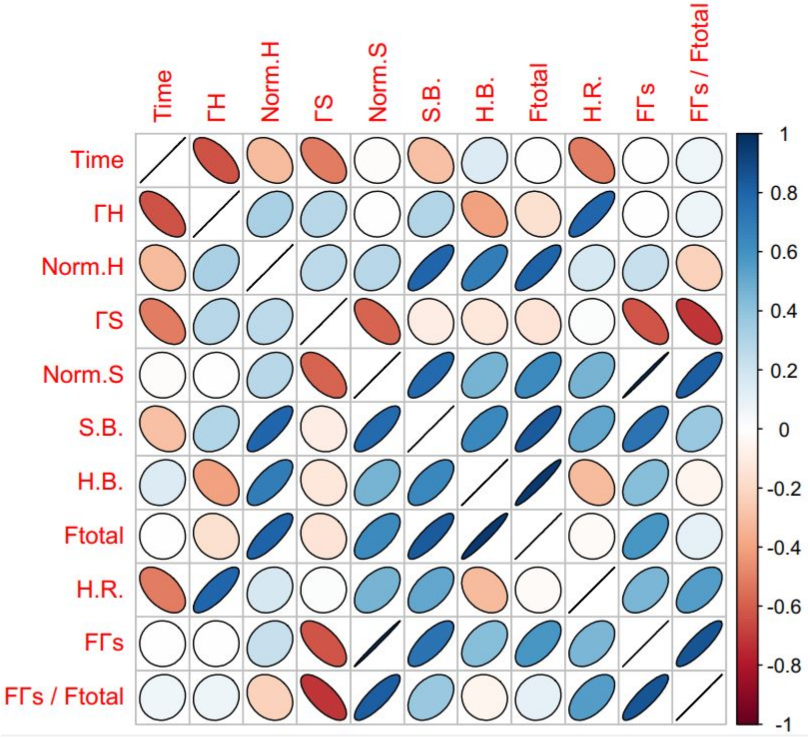

Figure 4.4: The correlation plot for the spectral parameters of the double power-law model fitted to the 27 spectra. The flatter the ellipses are in the plot, the stronger the correlations. If the ellipse is blue then the correlation is positive and if the ellipse is orange, then the correlation is negative.

The correlation plot in Fig. 4.4 shows correlations between different spectral parameters of the model. As shown in Fig. 4.4, there is strong negative correlation between the slope of the soft power law and it normalization. Therefore, this correlation was plotted in Fig. 4.5. The strong negative correlation in Fig. 4.5 shows a harder-when-brighter trend because as the slope of the power-law decreases, the flux in the hard band increases. However, AGN in which the dominant emission originates in the accretion disk show a softer-when-brighter trend instead. Hence, this provides further evidence that the emsision of 3C273 is not originating in the disk but, instead, could be coming from the jet. Also, since there was strong negative correlation between the flux coming from the soft power-law and the slope of the soft

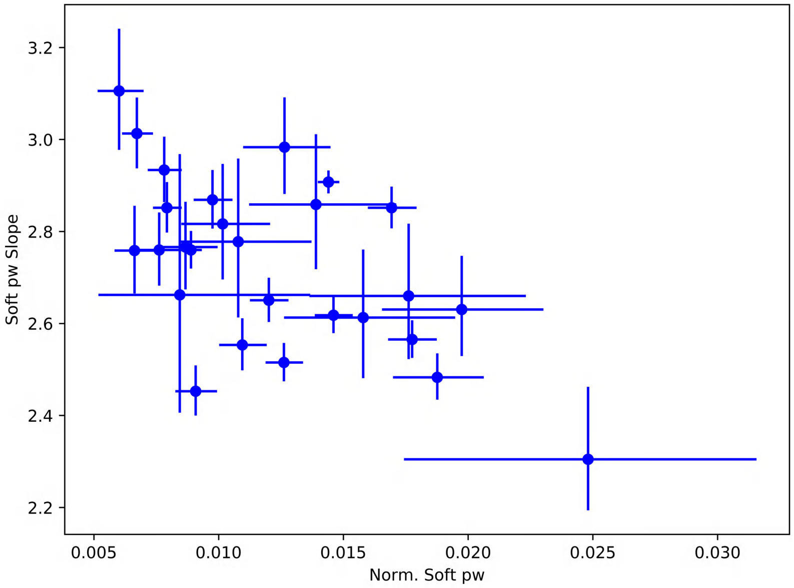

Figure 4.5: The negative correlation between the slope and normalization of the soft power-law

power-law, this was also plotted in Fig. 4.6.

Furthermore, since there is negative correlation between the time of the observations and Γ_{Hard}, Γ_{soft}, and the hardness ratio in Fig. 4.4, these three correlations were also plotted to investigate a possible trend.

The decrease in the two slopes of the double power-law and the hardness ratio of 0.3-0.8 keV flux to 2-10 keV flux suggests that the hard band flux (2-10 keV) may have increased over time.

4.4.2 Variability of Spectral Parameters

Finally, the variability of the double power-law over a period of 16 years was examined and is shown in Fig. 4.9. However, no particular trend was observed. Also, the fractional variability of the spectral parameters was calculated using Equations 3.2 and 3.3 and is shown in Fig. 4.10

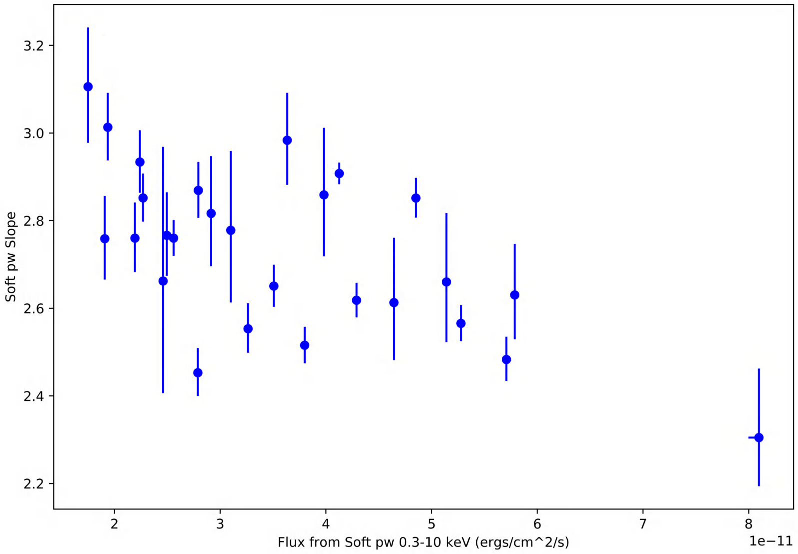

Figure 4.6: The negative correlation between the slope and the flux of the soft power-law

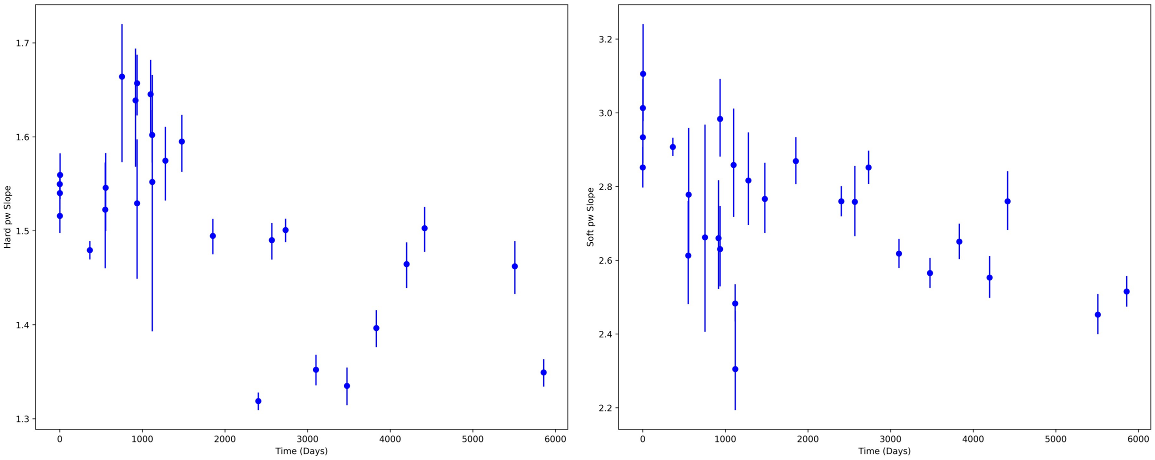

Figure 4.7: The slopes of the two power-laws have slightly decreased over a period of 16 years

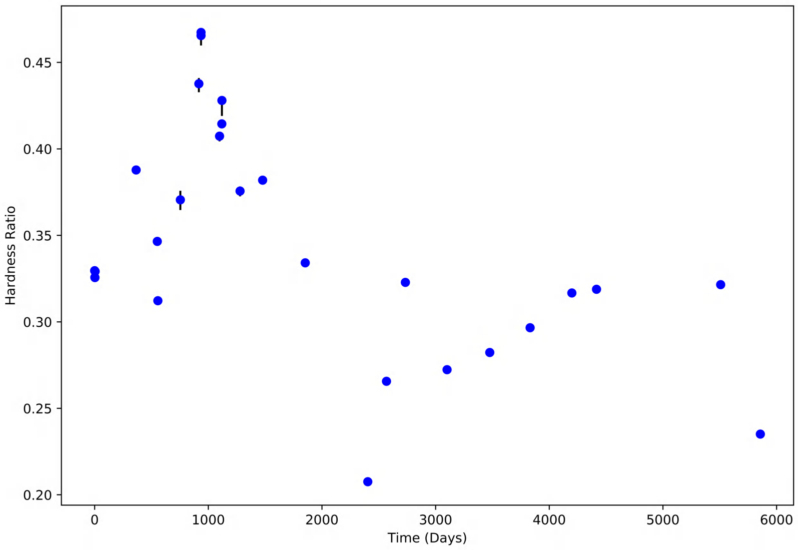

Figure 4.8: The decrease in the hardness ratio of 0.3-0.8 keV flux to 2-10 keV flux

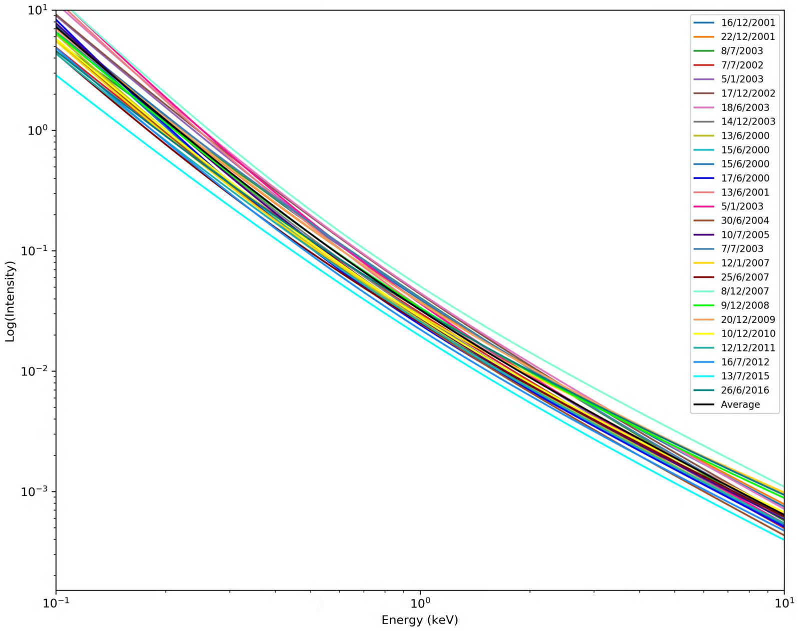

Figure 4.9: The variability of the double power-law with time

As can be seen from Fig. 4.10, the most variable parameters corrsponded to the soft power-law suggesting that the soft band of 3C273 is more variable than the hard band. Moreover, a similar behavior of the parameters was observed in the 2-10 keV modelling in Fig. 3.5 where the slope of the single power-law did not vary much but

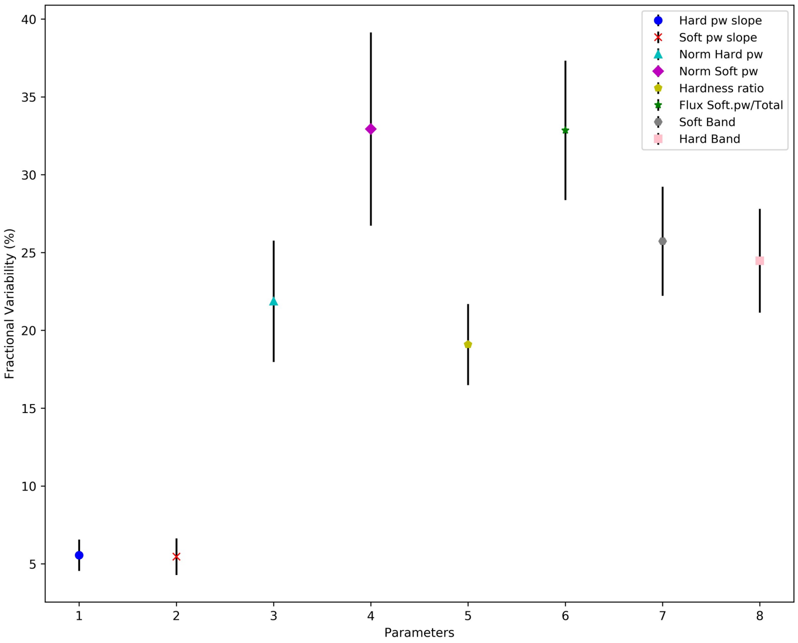

Figure 4.10: The variability of the spectral parameters of the double power-law model

the normalization did. In Fig. 4.10, the smallest fractional variability is that of the slopes while the normalizations are varying significantly.

Chapter 5

THE LEPTONIC RELATIVISTIC JET MODEL

The Leptonic Relativistic Jet Model in Xspec was used to study the physical parameters of the jet of 3C273. One of the reasons this model was chosen was because of the harder-when-brighter trend observed in the double power-law modelling in Fig. 4.5 which suggested that the x-ray emission of 3C273 in 0.3-10 keV range could be originating from the jet instead of coming directly from the accretion disk. The model is based on three papers which are Ghisellini and Tavecchio (2009), Ghisellini et al. (2010), and Gardner and Done (2017). Therefore these three papers were used to study and apply the jet model to the data. It has a total of 16 parameters listed in Table 5.1 that correspond to different physical parameters of the AGN and it can fit the x-ray spectra of different quasars by calculating the values of those parameters.

In order to fit the spectra of a particular jet, the model assumes the emitting region of the jet to be spherical with radius R_{diss} that is located at a distance Z_{diss} from the black hole and the two parameters are related by equation,

$$R_{diss} = \phi Z_{diss} \tag{5.1}$$

where ϕ is the opening angle of the jet in radians. Since Z_{diss} is the distance of the

Table 5.1: Description of the parameters of the Jet Model from Gardner and Done (2017), where parameters 8-14 are in the jet frame.

Parameter No.	**Parameter**	**Description of the parameter**
1	M_{BH}	Mass of the black hole in $M_{\odot}$
2	R_{co}	Comoving distance of the object in Mpc
3	$\log \dot{m}$	Logarithm of the mass accretion rate in units of L_d/L_{edd}
4	$\theta_{obs.}$	Inclination angle between the jet axis and the line of sight in units of degrees
5	Γ_{Bulk}	Bulk Lorentz factor of the jet
6	ϕ	Opening angle of the jet in radians
7	Z_{diss}	Distance of the dissipation region from the black hole in units of R_g
8	B	Magnetic field in the jet in units of Gauss
9	$\log P'_{rel.}$	Logarithm of the power injected in relativistic electrons in jet frame in units of $ergs^{-1}$. It determines the normalization of the spectrum.
10	γ_{min}	Minimum Lorentz factor of the injected electron distribution in the jet
11	γ_{break}	Break Lorentz factor of the inject electron distribution
12	$\gamma_{max.}$	Maximum Lorentz factor of the electron distribution in the jet
13	s_1	Slope of the electron distribution before the break
14	s_2	Slope of the electron distribution after the break
15	z	Redshift of the object
16	Norm.	Normalization constant which is always set to unity since the normalization is determined by parameter 9

dissipation region from the black hole where a fraction of the jet power is dissipated in the form of radiation, the contribution of different components of the AGN that are providing seed photons for external Compton are calculated depending on the value of Z_{diss} as shown in Fig. 5.1. The radii of BLR and Infrared (IR) torus in the model are scaled as the square root of the total accretion disk luminosity and are given by Equations 5.2 and 5.3 respectively.

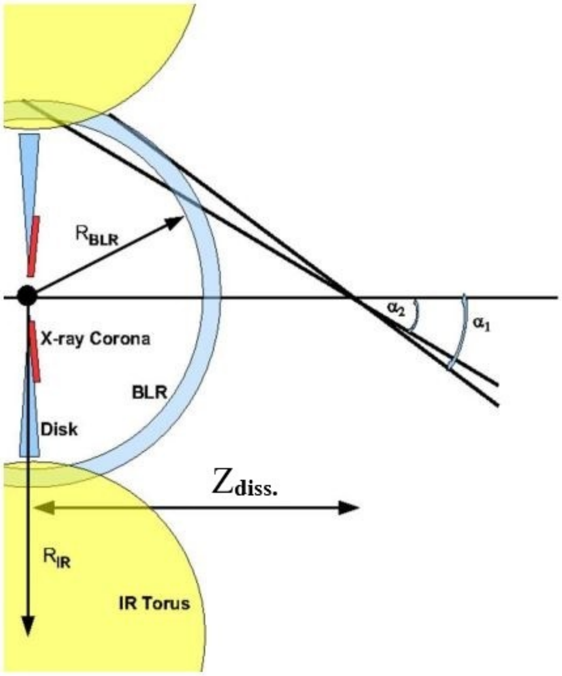

Figure 5.1: The radiation coming from the accretion disk, the X-ray corona, BLR, and IR torus provides seed photons for the dissipation region, and the contribution of the BLR is calculated from the angles at which the photons interact with dissipation region. Image Credit: Ghisellini and Tavecchio (2009)

$$R_{BLR} = 10^{17}\left(\frac{L_d}{10^{45} ergs^{-1}}\right)^{1/2} \text{cm} \tag{5.2}$$

$$R_{IR} = 2.5 \times 10^{18}\left(\frac{L_d}{10^{45} ergs^{-1}}\right)^{1/2} \text{cm} \tag{5.3}$$

The radiation that originates in the accretion disk is believed to be reprocessed in the BLR and the IR torus, and then reflected towards the dissipation region (Sect. 1.3.4). If $Z_{diss} < R_{diss}$ then U_{BLR} is the dominant seed photon density for the external comtpon effect. However if $Z_{diss} > R_{diss}$, then U_{IR} provides most of the seed photons for the external compton to take place in the jet. Apart from radiation coming from the BLR and IR torus, the model also calculates any seed photons coming directly from the disk and the X-ray corona.

Apart from the seed photon densities, the model calculates the logarithm of accretion rate, $\log \dot{m}$, shown in Table 5.1. If the value of parameter 3 is set below -2, then the model assumes radiatively inefficient accretion disk and therefore it does not take into account any radiation produced externally to jet but only calculates the radiation produced internally to the jet through SSC process (Sect 1.3.3). This type of emission with radiatively inefficient accretion disk is usually observed in BL Lac objects and hence it can also be used to study those objects. However if the value of parameter is $>$ -2, then it assumes that object is an FSRQ with a standard accretion disk, and so it calculates the contribution of external radiation in the spectrum along with the SSC contribution.

$$Q(\gamma) = Q_0 \frac{\left(\frac{\gamma}{\gamma_b}\right)^{-s_1}}{1 + \left(\frac{\gamma}{\gamma_b}\right)^{-s_1+s_2}} \tag{5.4}$$

Other than the accretion rate, the model assumes that the accelerated electrons in the jet follow a broken power-law distribution as shown in Equation 5.4, where the values for parameters in the equation are calculated from parameters 10 to 14 in

Table 5.1 and $\gamma_{min.} < \gamma < \gamma_{max.}$. γ_b is the break Lorentz factor where the electron distribution changes slope from s_1 to s_2. The value of the normalization constant Q_0 is determined by the the power injected into relativistic electrons (parameter 9, Table 5.1), and is related to it by equation,

$$P'_{rel.} = \frac{4\pi}{3} R_{diss}^3 m_e c^2 Q_0 \int_{\gamma_{min}}^{\gamma_{max}} \gamma \frac{\left(\frac{\gamma}{\gamma_b}\right)^{-s_1}}{1 + \left(\frac{\gamma}{\gamma_b}\right)^{-s_1+s_2}} d\gamma \tag{5.5}$$

However in order to calculate the Lorentz factor of the electrons once they cool off radiatively by losing energy in the dissipation region, the model first calculates the total seed photon density that would result in the inverse Compton effect taking place in the dissipation region that would cool off the electrons. This seed photon density is calculated based on the radiation produced internally to the jet and radiation coming from external components. The Lorentz factor of the cooled off electrons is then calculated by equation,

$$\gamma_{cool} = \frac{3 m_e c^2}{4 \sigma_t R_{diss} U'_{seed}} \tag{5.6}$$

where the $U_{seed} = U'_{synchrotron} + U'_B + U'_{external}$ in erg cm^{-3}.

Lastly, since the jet dissipates only a fraction of its total power in the form of radiation, there must be different components within the jet that are contributing to the total jet power. These components are the radiation power of the jet, P_r, the power carried by the magnetic field in the jet, P_b, the kinectic power of the electrons, P_e, and the kinetic power of the protons, P_p. The model calculates these components in the observers frame in units of $ergs^{-1}$ by equation,

$$P_i = \pi R^2_{diss.}\Gamma^2_{Bulk}\beta c U'_i \tag{5.7}$$

where $i = r, B, e, p$, and U_i is the energy density of the i^{th} component. Γ_{Bulk} is the Bulk Lorentz factor of the jet (parameter 5, Table 5.1), and $\beta = v/c$ where v is the velocity of the jet. Also, since the radiation coming from the jet undergoes Doppler boosting (Sect. 1.3.2), the Doppler boost factor, δ, is related to Γ_{Bulk} and inclination angle of the jet axis, $\theta_{obs.}$ by equation,

$$\delta = \left(\Gamma_{Bulk} - cos(\theta_{obs.})\sqrt{\Gamma^2_{Bulk} - 1}\right)^{-1} \tag{5.8}$$

Chapter 6

Applying jet Model to 3C273

The Leptonic Jet Model was applied to 3C273 in the multi-wavelength band to the data obtained from the large area telescope (LAT) on board the Fermi satellite and the data from the Swift satellite in Ghisellini et al (2010). Fig. 6.1 shows the the spectral energy distibution (SED) obatined by applying the model to that data where the contributions of emission from different regions of the AGN are shown. The values for different parameters of the jet model fitted to the multiwavelength spectra of 3C273 were reported in the paper and those values were used to apply the jet model

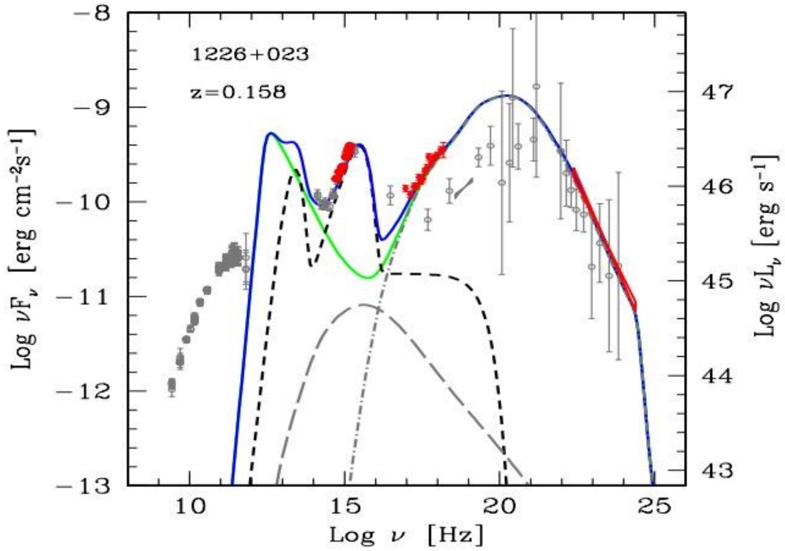

Figure 6.1: The overall emission of 3C273 in the multiwavelength band where the short dashed line is the emission from IR torus, accretion disk, and x-ray corona. The long dashed line is the emission from SSC process, and dotted line is the EC contribution. The green line shows the flux from the jet, and the blue line is the total sum of different components of the emission. Image Credit: Ghisellini et al (2010)

Table 6.1: The values used for the jet model parameters from Ghisellini et al (2010)

Model parameter No.	**Value from previous work**
01	$8 \times 10^8\ M_\odot$
02	679 Mpc (Taken from NED Extragalactic database)
03	-0.39794
04	3^o
05	12.9
06	0.1 rad
07	1000 R_g
08	11.6 Gauss
09	43.2
10	1
11	40
12	2×10^4
13	1
14	3.4
15	0.158

to the data for this work. However, the application of the model was different in this work from the Ghisellini et al (2010), since for this work the Xspec package was used to fit the jet model to the 27 spectra of the object whereas in that paper the jet model was not present in the Xspec at the time and therefore different softwares were used. The values for different parameters taken from the previous work are shown in Table 6.1.

6.1 SPECTRUM 13 ANALYSIS

To study how the jet model can be applied to the data of 3C273, the spectrum with the highest spectral data counts (SDC) was used which was spectrum 13. This is because spectrum 13, as mentioned earlier, was the hardest spectrum to fit with any model in chapter 4 due to its high quality data points. Hence in order examine how the values of the parameters from previous work go with the best quality data, a thorough analysis on spectrum 13 were carried out.

However, due to time constraint, not all 16 paramters could be fitted to the spectrum at once in Xspec because the more number of parameters that were allowed to run free in the simulations, the more time consuming the model simulations became. Other than time constraint, one of goals of the physical modelling were to find the model that can fit the data with the least number of parameters.

6.1.1 Fitting Different Parameters

In order to fit the spectra with the simplest type of model or least number of parameters, different combinations of the parameters in Table 5.1 were used, and the fits of spectrum 13 with those combinations of parameters were examined by using the $\frac{data}{model}$ ratio line in the Xpsec plots and determining the reduced χ^2 values of the fits.

However, not all the parameters of model were examined in this way. This is because mass of black hole, M_{BH}, the comoving distance of the object, R_{co}, the inclination angle of the jet axis, $\theta_{obs.}$, the opening angle of the jet, ϕ, and the redshift, z, are the parameters that are not expected to vary significantly over a time span of 16 years. Therefore, while finding the best combination of parameters for the jet model, these parameters were frozen in the simulations with their respective values listed in Table 6.1 throughout the analysis for finding the best parameter combination. Also, the Galactic absorption of $N_H = 1.77 \times 10^{20}$atoms cm^{-2} was included in the simulations which was also not varied.

To start with the simplest type of model, one parameter from Table 5.1 was fitted

Table 6.2: Fits of spectrum 13 with different combinations of the parameters

Fitted Parameters no.	**Reduced χ^2 values of the fits**
03	609.4868
05	180.8452
08	24495.39
09	231.6118
10	372.687
11	195.5075
12	31747.10
13	8014.649
14	11468.10
05, 03	40.35392
05, 08	229.1767
05, 09	35.52486
05, 10	272.5662
05, 11	108.7191
05, 12	179.835
05, 13	182.3922
05, 14	12.2621
09, 03	229.5193
09, 08	504.1868
09, 10	195.0449
09, 11	281.3732
09, 12	231.2464
09, 13	231.7303
09, 14	14.03748
05, 11, 14	4.63633
05, 09, 11, 14	4.85638
03, 05, 11, 14	9.684436
05, 10, 11, 14	4.71037
05, 09, 10, 11, 14	5.206020
03, 05, 09, 11, 14	1.38111

at a time while the other 15 parameters were frozen in the simulations with their respective values in Table 6.1. The reduced χ^2 values of the fits obtained with the fitted parameters are shown in Table 6.2. As can be seen from the reduced χ^2 values in the table above, one parameter is unable to fit the spectrum of 3C273. Hence the parameters which gave the lowest χ^2 values, which were parameters 05 and 09 were taken, and the combinations of these two parameters with all the other parameters were tested as can be seen in the next two sections of Table 6.2. The lowest χ^2 values achieved by fitting two parameters at a time with different combinations involved parameters 03, 05, 09, 11, and 14 as can be seen in the middle two sections of Table 6.2.

Hence, different combinations with these parameters were tested in the last section of Table 6.2 with first three parameters at a time, then four parameters, and then finally when the five parameters were fitted together, they gave the best fit of spectrum 13. Therefore these 5 parameters were chosen to fit all the 27 spectra of 3C273 while all the other parameters were frozen.

Also, of the five parameters, three parameters which are 09, 11, and 14 are related to the electron distribution within the jet as can been seen from Table 5.1. Therefore, this suggests that the shape of the overall emission of 3C273 in the x-ray band is most probably determined by the electron distribution in the jet.

6.1.2 FITTING DIFFERENT MASSES

In section 1.5, the value for the mass of the black hole in the center of 3C273 was $5.0 \times 10^9 M_\odot$ (Husemann et al, 2010). In fact, most of the literature values report the mass of 3C273 to be on the order of $10^9 M_\odot$, but as can be seen in Table 6.1, the value taken for the mass of 3C273 was $8 \times 10^8 M_\odot$. Therefore, in order to get as accurate results as possible, another analysis on spectrum 13 were carried out to find the best fit mass value of 3C273 for the jet model. Since the combination of parameters that were allowed to vary in the simulations was already known, the values for these were to be calculated from the simulations. However, the values of the parameters that

Table 6.3: Mass analysis of spectrum 13

χ^2	$M_{BH}(M_\odot)$	$Z_{diss.}(R_g)$	ϕ (rad)	B (Gauss)
2580.70	8×10^8	1000	0.100	11.600
2868.38	9×10^8	1125	0.089	10.937
2711.91	1×10^9	1250	0.080	10.375
2344.39	2×10^9	2500	0.040	7.336
2340.07	3×10^9	3750	0.027	5.990
2338.62	4×10^9	5000	0.020	5.188
2337.60	4.6×10^9	5750	0.017	4.838
2339.42	5×10^9	6250	0.016	4.640
2361.99	6×10^9	7500	0.013	4.235
2550.92	7×10^9	8750	0.011	3.922
3062.94	8×10^9	10000	0.010	3.668

were frozen during the analysis, corresponded to a black hole mass of $8 \times 10^8 M_\odot$, and so in order to find the values for the parameters 06, 07, and 08, in Table 5.1, the scaling Relations 6.1, 6.2, and 6.3 were used respectively, (Gardner and Done, 2017).

$$\phi \propto \frac{1}{Z_{diss.}} \tag{6.1}$$

$$Z_{diss} \propto M_{B.H.} \tag{6.2}$$

$$B \propto \frac{1}{\sqrt{M_{BH}}} \tag{6.3}$$

As for the values of parameters 02, 04, 10, 12, 13, and 15, the same values as in Table 6.1 were used since these parameters are not expected to vary significantly with changing M_{BH}. The results of the analysis for different values of M_{BH} are shown in Table 6.3 along with the χ^2 values of the fits.

The Lowest χ^2 value was achieved for $M_{BH} = 4.6 \times 10^9\ M_\odot$, and therefore this value, along with its corresponding values for parameters 06, 07, and 08 in Table 6.3

were used to fit all the 27 spectra of 3C273.

6.2 Results and Analysis

With the combination of the 5 parameters and the best fit value for M_{BH} found in the previous sections, the jet model was applied to all the 27 spectra in the 0.3-10 keV band, and the fits for the six spectra with the highest SNR are shown in Fig. C.5, and the data for the fits is shown in Tables 6.4 and 6.5.

Since the model was able to successfully fit all the spectra with the highest reduced χ^2 value being 1.4, a correlation analysis were performed on different parameters of the model as shown in Fig. 6.2.

Table 6.4: Fitted parameter values of Jet Model

Spectrum Number	**Reduced χ^2**	$\log \dot{m}$	Γ_{bulk}	$\log P'_{rel.}$	γ_{b}	S_2
09	1.12	$-0.0289^{+0.0004}_{-0.0004}$	$6.336^{+0.002}_{-0.002}$	$43.8500^{+0.0004}_{-0.0004}$	$112.7^{+0.1}_{-0.1}$	$3.745^{+0.002}_{-0.002}$
13	1.21	$-0.0447^{+0.0004}_{-0.0004}$	$6.837^{+0.002}_{-0.002}$	$43.8792^{+0.0003}_{-0.0003}$	$153.33^{+0.09}_{-0.09}$	$4.674^{+0.002}_{-0.002}$
17	1.22	$-0.055^{+0.007}_{-0.001}$	$7.487^{+0.002}_{-0.002}$	$43.6927^{+0.0003}_{-0.0003}$	$133.4^{+0.2}_{-0.2}$	$3.311^{+0.002}_{-0.002}$
18	1.43	$-0.0499^{+0.0002}_{-0.0003}$	$11.202^{+0.001}_{-0.005}$	$43.3381^{+0.0003}_{-0.0003}$	$185.1^{+0.3}_{-0.2}$	$4.444^{+0.006}_{-0.007}$
20	1.11	$-0.0343^{+0.0005}_{-0.0005}$	$7.840^{+0.002}_{-0.002}$	$43.8181^{+0.0003}_{-0.0003}$	$123.2^{+0.1}_{-0.1}$	$3.820^{+0.002}_{-0.002}$
27	1.21	$0.0362^{+0.0003}_{-0.0003}$	$8.581^{+0.003}_{-0.003}$	$43.4754^{+0.0003}_{-0.0003}$	$185.7^{+0.4}_{-0.4}$	$3.691^{+0.005}_{-0.005}$

As shown in the correlation plot of the jet, there were a number of strong correlations both, negative and positive, that were found after performing the correlation analysis on all the calculated parameters of the model. However, the correlations

Table 6.5: Jet Model flux where all the flux values are in units of erg cm^{-2} s^{-1}

Spectrum Number	**Soft Band Flux(0.3-0.8 keV)** 10^{-11}	**Hard Band Flux (2-10 keV)** 10^{-11}	**Flux (0.3-10 keV)** 10^{-11}	**Hardness Ratio** $\left(\frac{\text{SoftBand}}{\text{HardBand}}\right)$
09	2.67	8.10	13.78	0.33
13	3.77	9.70	17.12	0.39
17	4.08	9.82	18.27	0.41
18	2.69	12.83	19.05	0.21
20	5.18	16.03	26.93	0.32
27	3.01	12.76	19.64	0.24

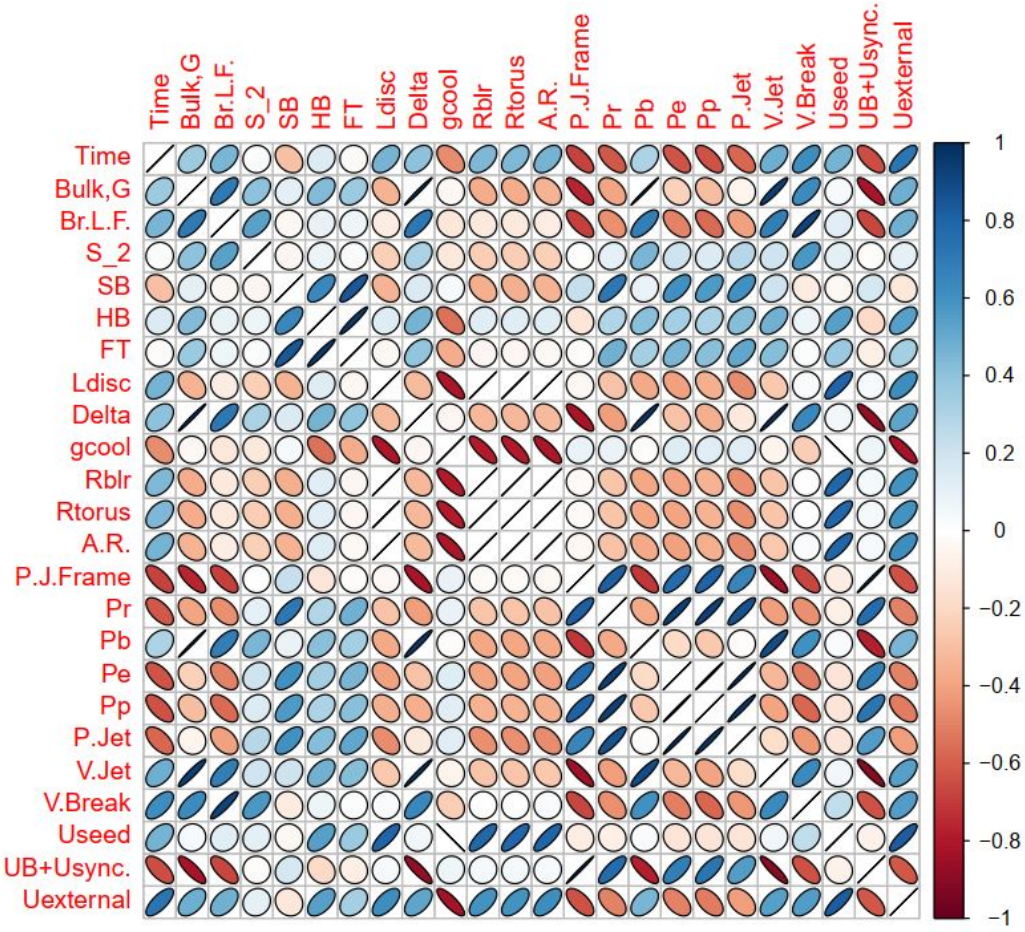

Figure 6.2: Correlation plot for different parameters of the Jet model of 3C273. The descriptions for different labels on this plot are given in Table C.1 in the appendix.

that were of main focus in this work were the ones that involved the soft band, hard band, different seed photon densities, accretion rate, and power components of the jet. Other than that, many correlations between different parameters were expected since they arise from the equations which relate those parameters and were discussed in chapter 5.

The strong, positive correlation found between the soft band of the flux and radiation power of the jet supported the result of Fig. 4.5, which suggested that the soft x-ray emission of 3C273 was coming from the jet instead of accretion disk. Hence soft band flux was plotted against the radiation power of the jet in Fig. 6.3.

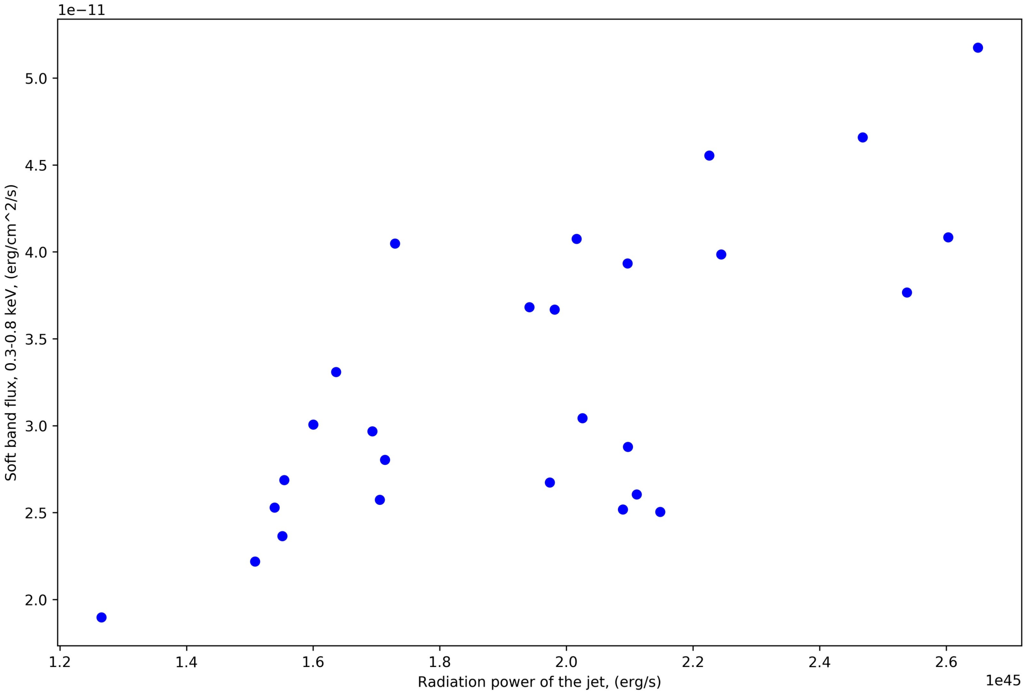

Figure 6.3: The positive correlation between the soft band and radiation power of 3C273

Although the correlation plot in Fig. 6.2, also shows a positive correlation between the hard band flux and the external seed photon density, the correlation was not as strong as the one in Fig. 6.3, and therefore was not investigated in detail. However, since the external seed photon density suggested a possible relation between the hard band and external Compton, the hard power-law slope from the double power-law model was plotted against the external seed photon density. Furthermore, the soft power slope from the double powerlaw model was plotted against the SSC seed photon density to investigate any possible relations.

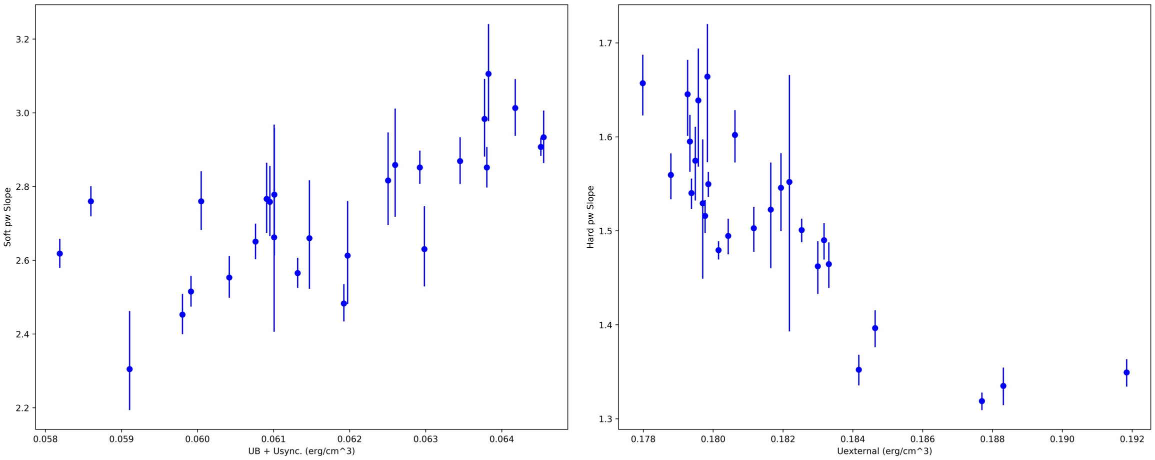

Figure 6.4: The slopes of the double power law model were plotted against the SSC and external seed photon densities calculated from the jet model to examine the possible relations.

Since positive and negative correlations were found between Γ_{soft} and $(U_B+U_{sync.})$, and Γ_{Hard} and $U_{external}$, respectively, the relation between the slopes and photon densities were investigated further by plotting them vice-versa. The Γ_{Hard} was plotted against SSC photon density and Γ_{soft} was plotted against external photon density. However, this time no strong correlations were observed as in Fig. 6.4 and therefore were not investigated in detail. Also, as can be seen in the correlation plot in Fig. 6.2, the seed photon density for SSC, $(U_B + U_{sync.})$, has a negative correlation with time while the $U_{external}$ has a positive correlation with time, these two trends were also invesitgated and are shown in Fig. 6.5. Lastly, the components of the jet power for

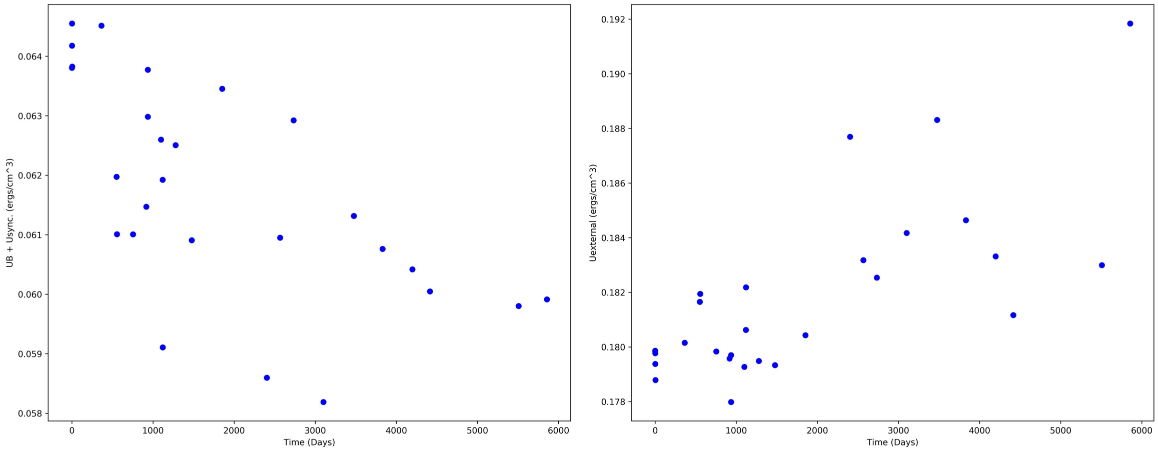

Figure 6.5: The seed photon density for SSC process in the jet has decreased over time while the EC seed photon density has increased over time.

3C273 have decreased over time, except the magnetic field component which does not show any particular trend, while the accretion rate and the components associated with the accretion disk have increased over time. Hence, these trends were also examined and are shown in Fig. 6.6.

6.2.1 Variability of the fitted Parameters

Finally, the fractional variability of the five fitted parameters was calculated using Equations 3.2 and 3.3. The most variable parameter over the period of 16 years was parameter 09 in Table 5.1 which corresponded to the power injected in the relativistic electrons in jet frame with a variability of about 34 percent as shown in Fig. 6.7 while the least varying parameter were the accretion rate and the slope of the electron distribution in the jet.

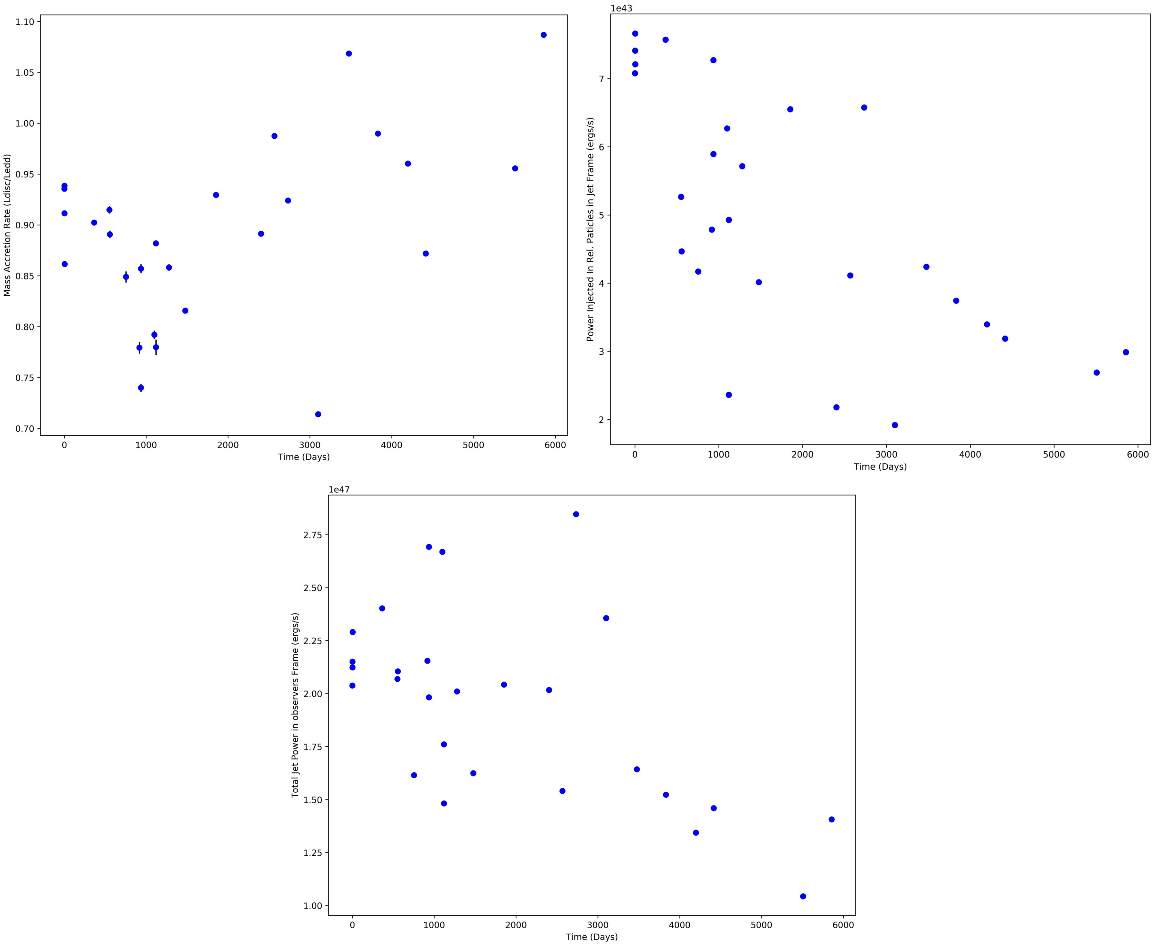

Figure 6.6: The accretion rate has increased over time while the power in the jet has decreased with time.

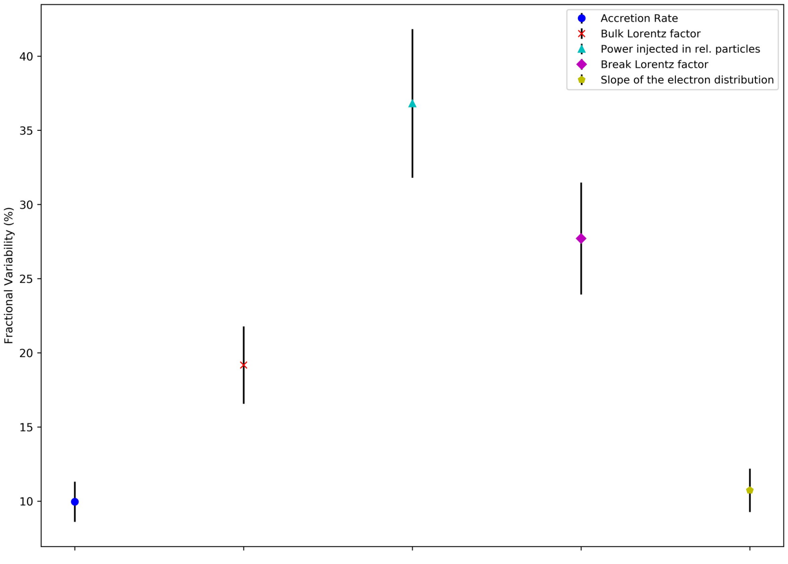

Figure 6.7: Fractional variability of the fitted parameters for the jet model.

Chapter 7

Discussion

The nature of the soft band, 0.3-0.8 keV, observed in the double power law modelling and the jet modelling shows that the emission of the soft band is coming from the jet and most probably arising from the SSC process taking place within the jet. This is because the harder when brighter trend in Fig. 4.5 suggested that the soft X-ray emission was coming from the jet and then a strong positive correlation was observed between the soft band flux and radiation power of the jet in Fig. 6.3. Furthermore, in Fig. 6.4, the seed photon density for the SSC process calculated from the jet model had a strong positive correlation with the slope of the soft power-law that was calculated from the double power-law model which shows that the higher the SSC seed photon density is, the steeper the soft power-law gets, and the higher the soft band flux becomes. Thus these observations involving the soft X-ray band provide strong evidence that the soft band emission of 3C273 in 0.3-0.8 keV range is originating in the jet through the synchrotron self-Compton effect.

As for the hard band in 2-10 keV range, the harder when brighter trend observed in Fig. 4.5 also suggested that the hard band flux was increasing with decreasing slope. Moreover, the hard band slopes from the single power law modelling and the double power-law modelling were observed to have decreased over the period of 16 years as can be seen from Fig. 3.4 and 4.7. Also, Fig. 4.8 showed that the hardness ratio from the double power-law modelling decreased over time. These decreasing trends hint at the possibility that the hard band strength has increased over time. Fig. 6.5 further emphasizes on this idea since the seed photon density for the external Compton effect in the plot has increased with time. Furthermore, in Fig. 6.4, the negative correlation between the hard power law slope from the double power-law model and the external seed photon density from the jet model suggests that the hard band, 2-10 keV, could be originating due to EC effect taking place in the jet. This is because the negative correlation means that the more external seed photons that are the present, the less steep the slope of the hard power-law gets which results in a higher hard band flux. Hence, these observations involving the hard band flux suggest that it is most probably originating due to the external Compton effect taking place in the jet and since the external seed photon density has increased with time as shown in Fig. 6.5, it would explain the decrease in the power slopes in Fig. 3.4 and 4.7, and the hardness ratio in Fig. 4.8.

Apart from that, in Fig. 6.6, it was observed that the jet power has decreased over time along with the injected power in the relativistic electrons while the accretion rate has increased with time and this hinted at a possible negative relation between the total jet power and the accretion rate. However, a strong negative correlation between the two parameters was in fact not observed when investigated in detail. Although a flat, orange ellipse in Fig. 6.2 is present between the accretion rate and the total jet power, the correlation was weak when plotted in scatter plot with a negative correlation coefficient of less than 0.5, and thus did not hint at a possible direct, negative relation between the accretion rate and jet power. Therefore, one possible explanation can be the link between the cooling of the energetic electrons within the jet due to the increase in the accretion rate and so external seed photons which would result in more electrons loosing their energies radiatively within the jet and hence resulting in the loss of total jet power. This is because from the hard band analysis discussed above, there is strong evidence that the EC effect is taking place in the jet and since the external seed photon density has increased as shown in Fig. 6.5, it could be that more relativistic electrons are loosing their energy via EC effect which is resulting in the overall loss of jet power.

Finally, as shown in Fig. 6.2, the velocity of the jet has a positive correlation with time suggesting that the velocity may have increased over time. Although this trend was not as strong when plotted, the velocity of the jet, however, was observed to have slightly increased over time, and since we know that accretion rate has also increased with time, this suggests at a possible relation between the two parameters. However, a positive correlation between these two parameters was also not observed that would hint at any direct relation between them. Therefore, one possible explanation of the velocity of the jet and accretion rate increasing simultaneously with time can be that as the black hole at the center accretes mass at an increasing rate, it also ejects some of that mass back into space at an increasing rate which would accelerate the jet.

Chapter 8

CONCLUSIONS

Based on the analysis of the seed photon densities that are produced externally and internally to the jet, it can be conculded that the soft x-ray band in 0.3-0.8 keV range is originating in the jet through the SSC process while the hard x-ray band in 2-10 keV range is originating in the jet due to the EC effect. Therefore, this may explain why a double power-law model accounting for two non-thermal emission processes was required to fit the data. Also, the accretion rate of 3C273 has been observed to be increasing with time while the total jet power along with its components is decreasing with time. Furthermore, the velocity of the jet has icreased with time suggesting that the jet of 3C273 may be accelrating.

Appendix A

Data

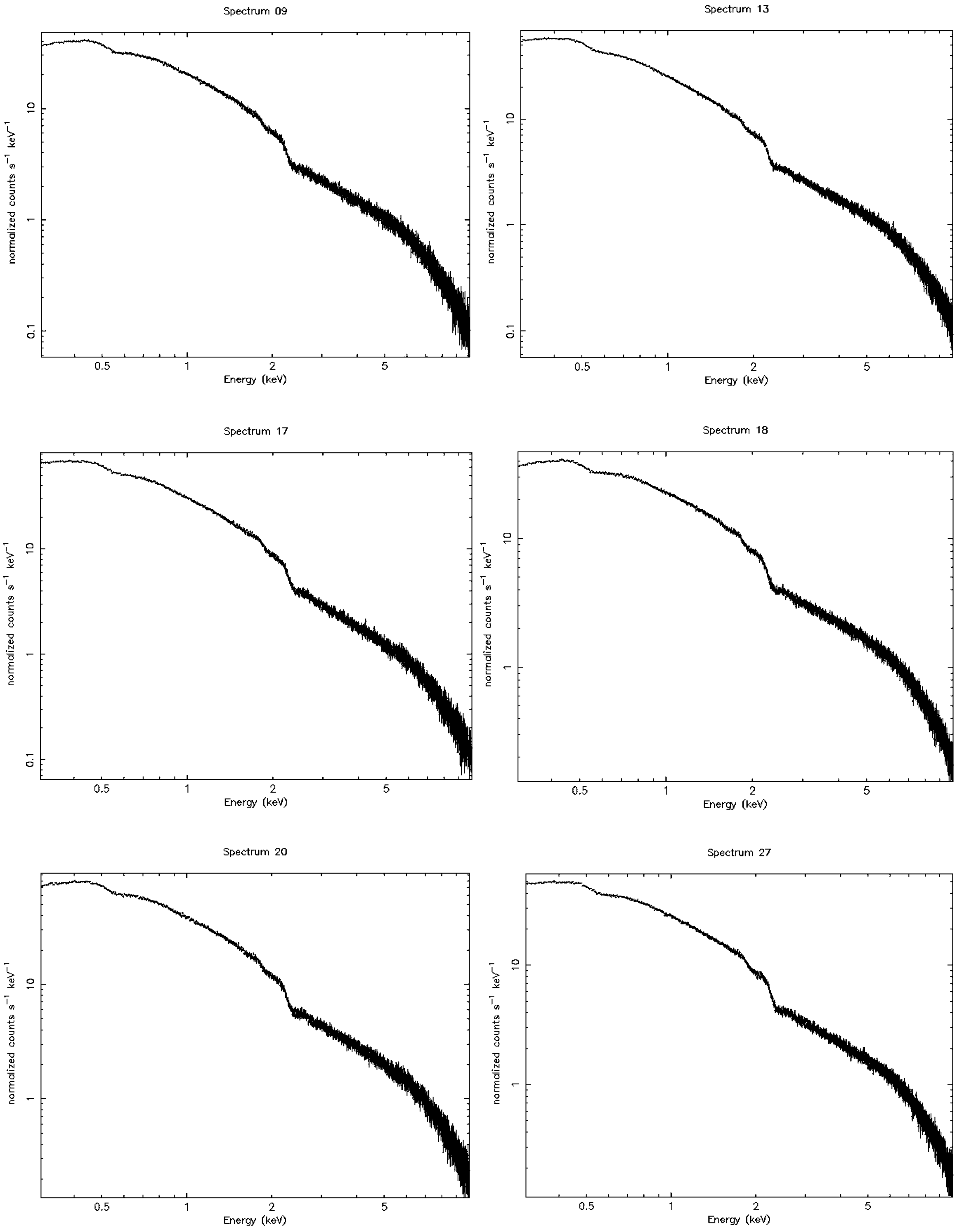

Figure A.1: The data in 0.3-10 keV band of six spectra with highest SNR

Appendix B

2-10 keV Modelling

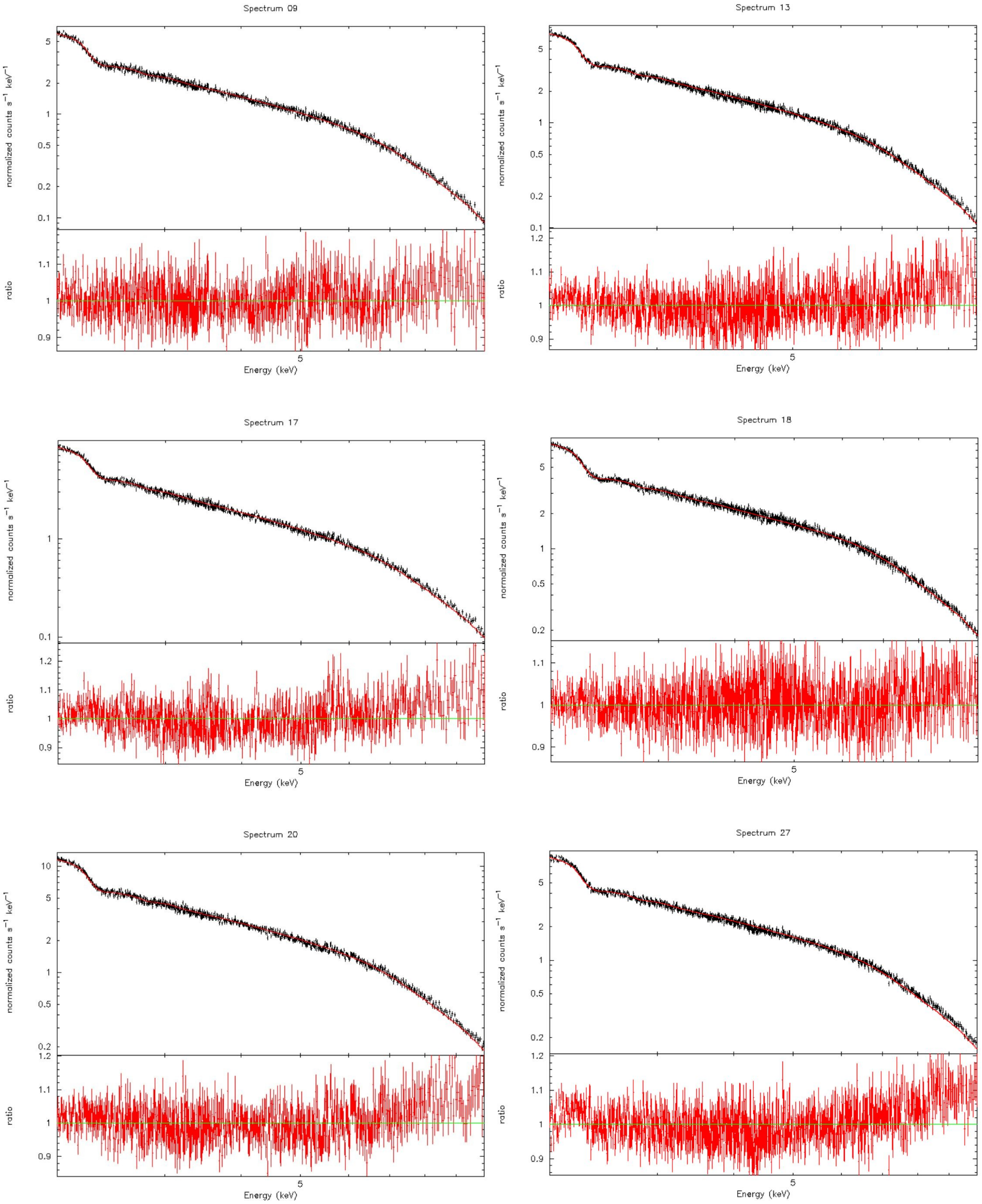

Figure B.1: Broken power-law fits for 2-10 keV modelling

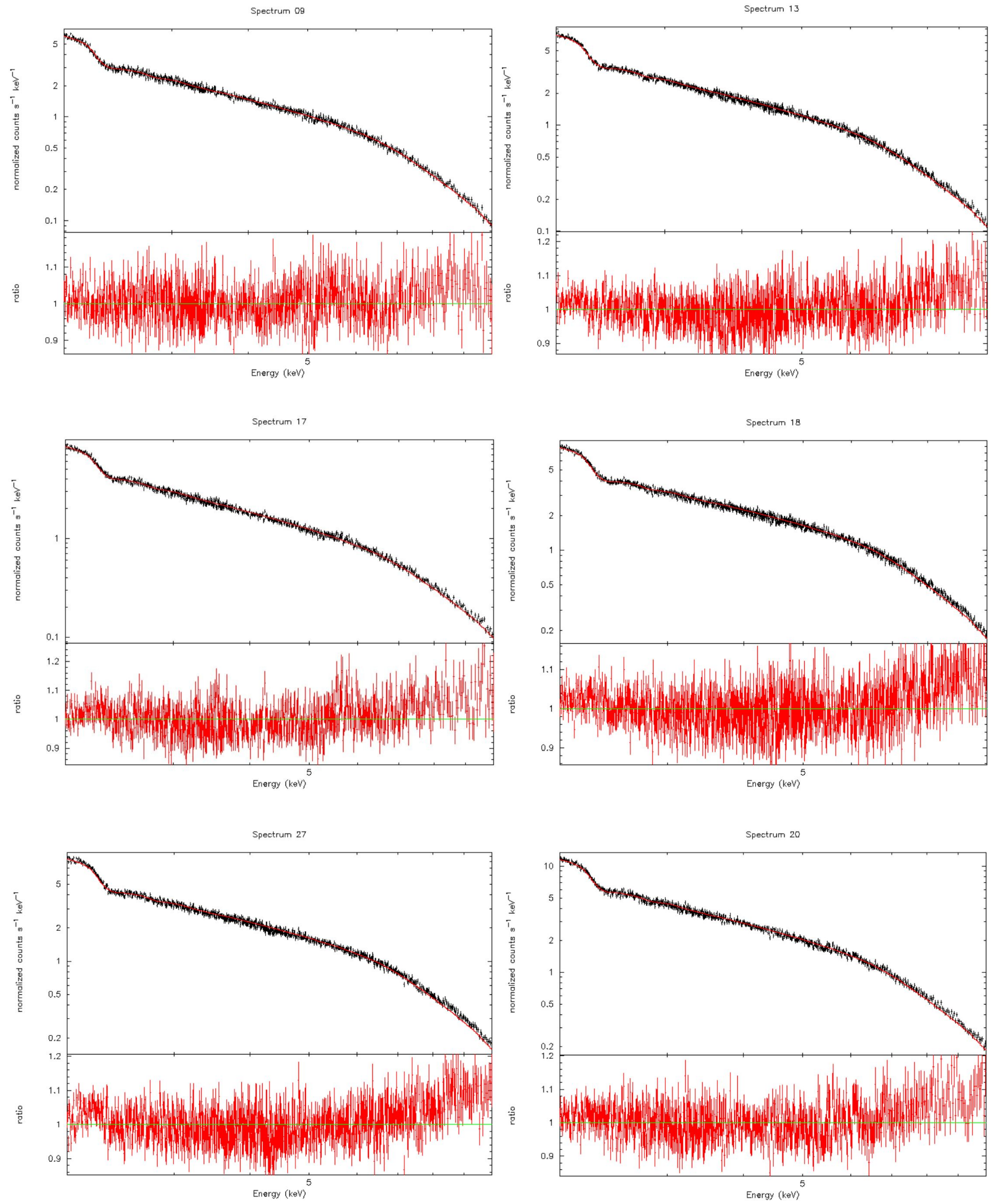

Figure B.2: Single power-law fits for 2-10 keV modelling

Appendix C

0.3-10 keV Modelling

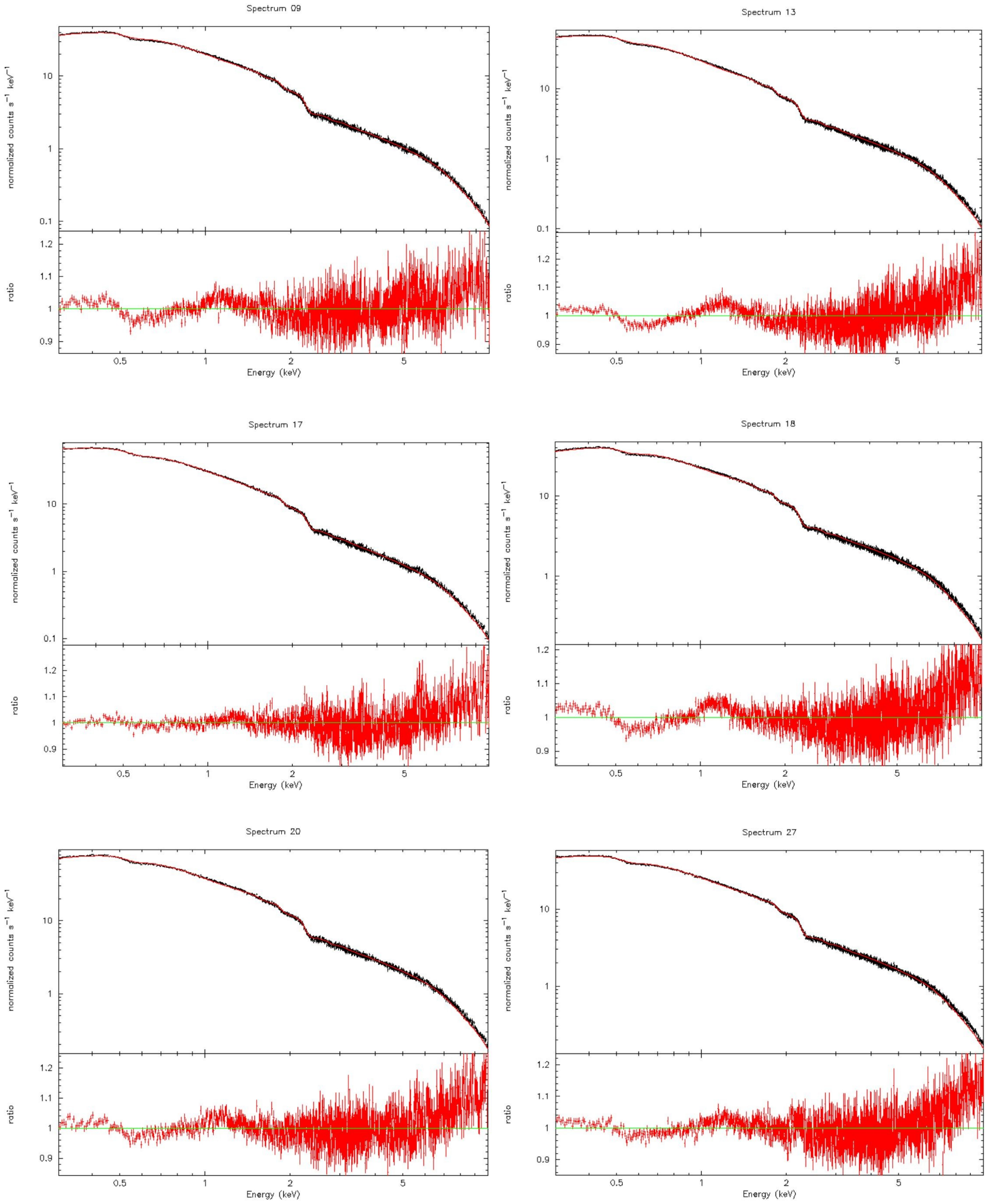

Figure C.1: Broken Power-law fits for 0.3-10 keV

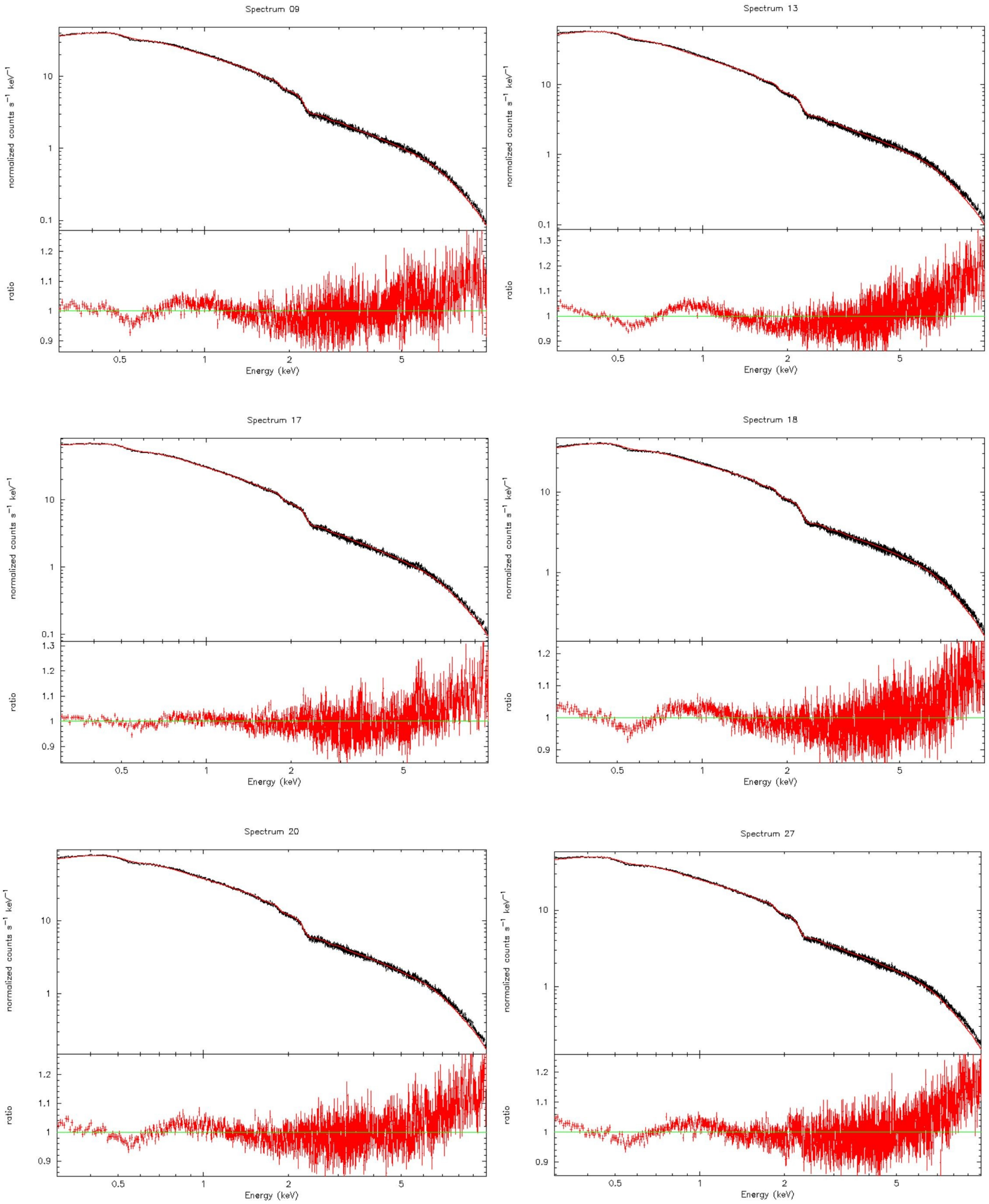

Figure C.2: Power-law + Blackbody fits

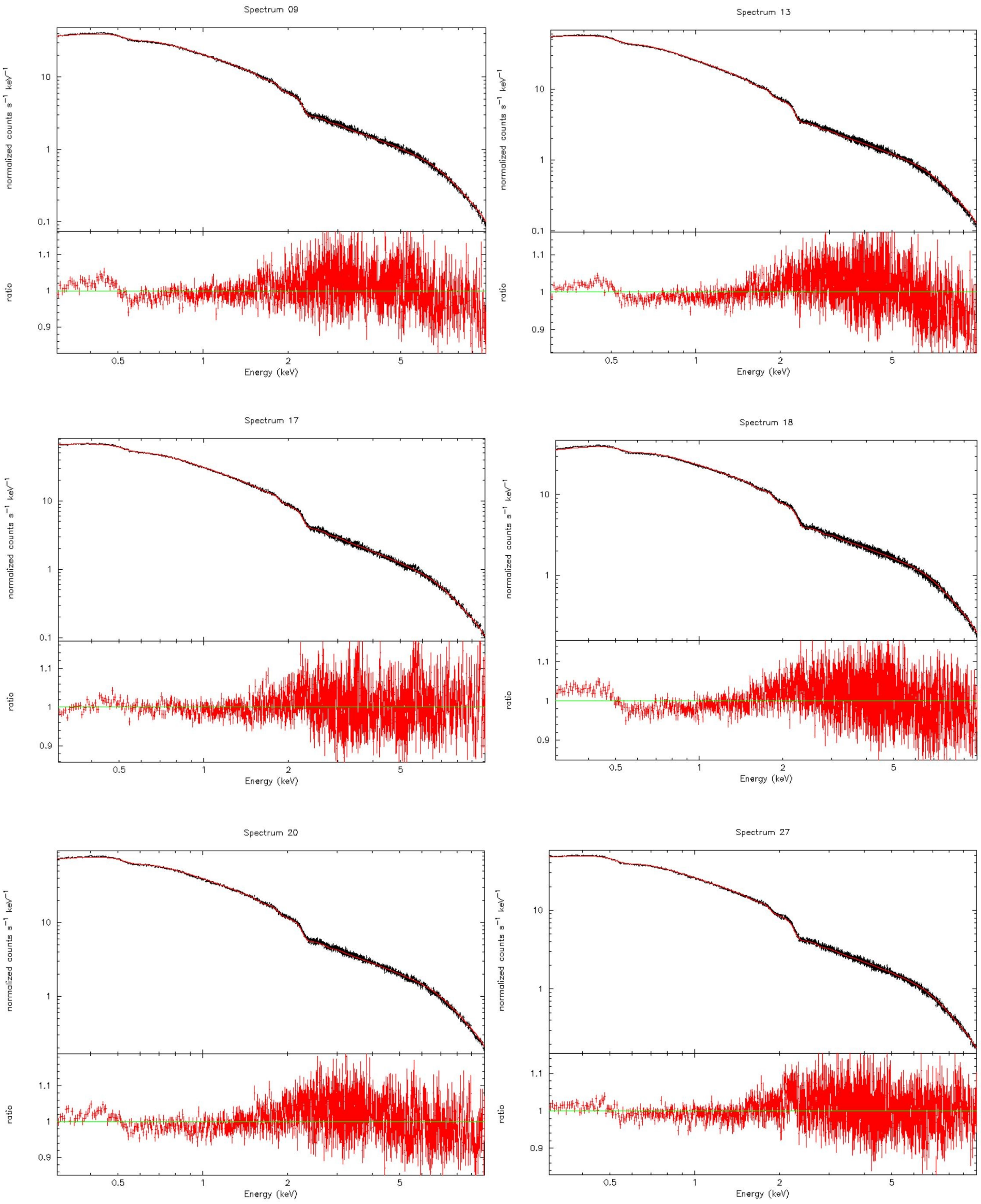

Figure C.3: Log-parabola fits

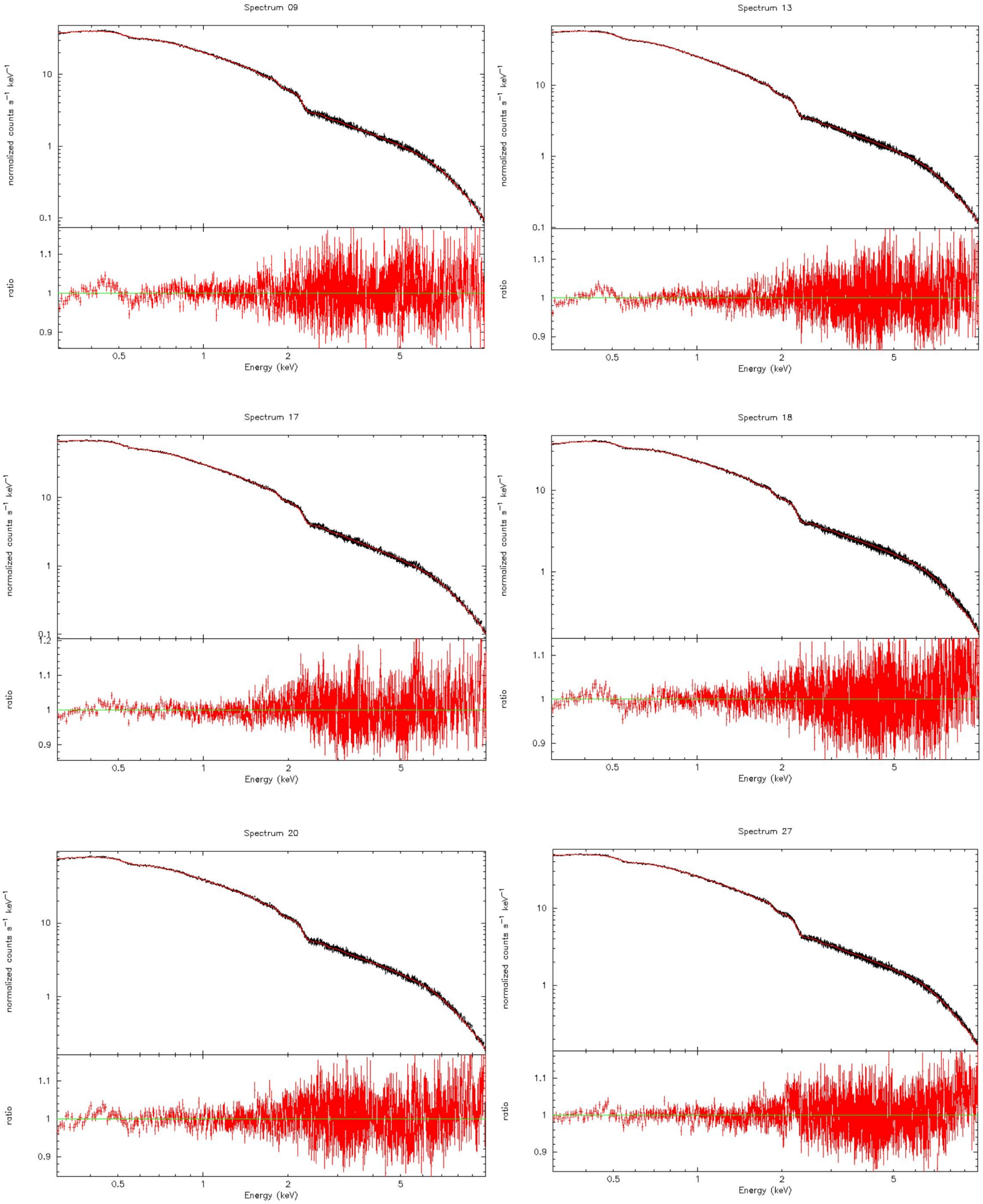

Figure C.4: Double power-law fits

Table C.1: Description of the labels that were given to the parameters calculated from the jet model in Fig. 6.2

Label on Fig. 6.2	**Description of the label**
Bulk, G	Bulk Lorentz factor of the jet
Br.L.F	Break Lorentz factor of the electron distribution
S_2	Slope of the electron distribution after the break
SB	Soft band of the flux in 0.3-0.8 keV range in units of erg cm^{-2} s^{-1}
HB	Hard band of the flux in 2-10 keV range in units of erg cm^{-2} s^{-1}
FT	Total flux from the jet model in 0.3-10 keV band in units of erg cm^{-2} s^{-1}
Ldisc	Luminosity of the accretion disk in units of erg s^{-1}
Delta	Doppler boost factor of the jet
gcool	Lorentz factor of the electrons that cool off radiatively in the jet
Rblr	Radius of the BLR from center of the AGN in units of R_g
Rtorus	Radius of the torus from the center of AGN in units of R_g
A.R.	Accretion rate of the disk
P.J.Frame	Power injected in the relativistic electrons in the jet frame in units of erg s^{-1}
Pr	Radiation power of the jet in units of $ergs^{-1}$
Pb	Power in the magnetic field in the jet in units of erg s^{-1}
Pe	Kinetic Power of the electrons in the jet in units of erg s^{-1}
Pp	Kinetic power of the protons in the jet in units of erg s^{-1}
P.Jet	Total power of the jet in units of erg s^{-1}
V.Jet	Velocity of the jet in units of C
V.Break	Break velocity of the electron distribution in the jet in units of C
Useed	Total seed photon density from radiation produced internally and externally to the jet
UB+Usync.	Seed photon density for synchrotron self-Compton in the jet
Uexternal	Seed photon density provided by radiation produced externally to the jet

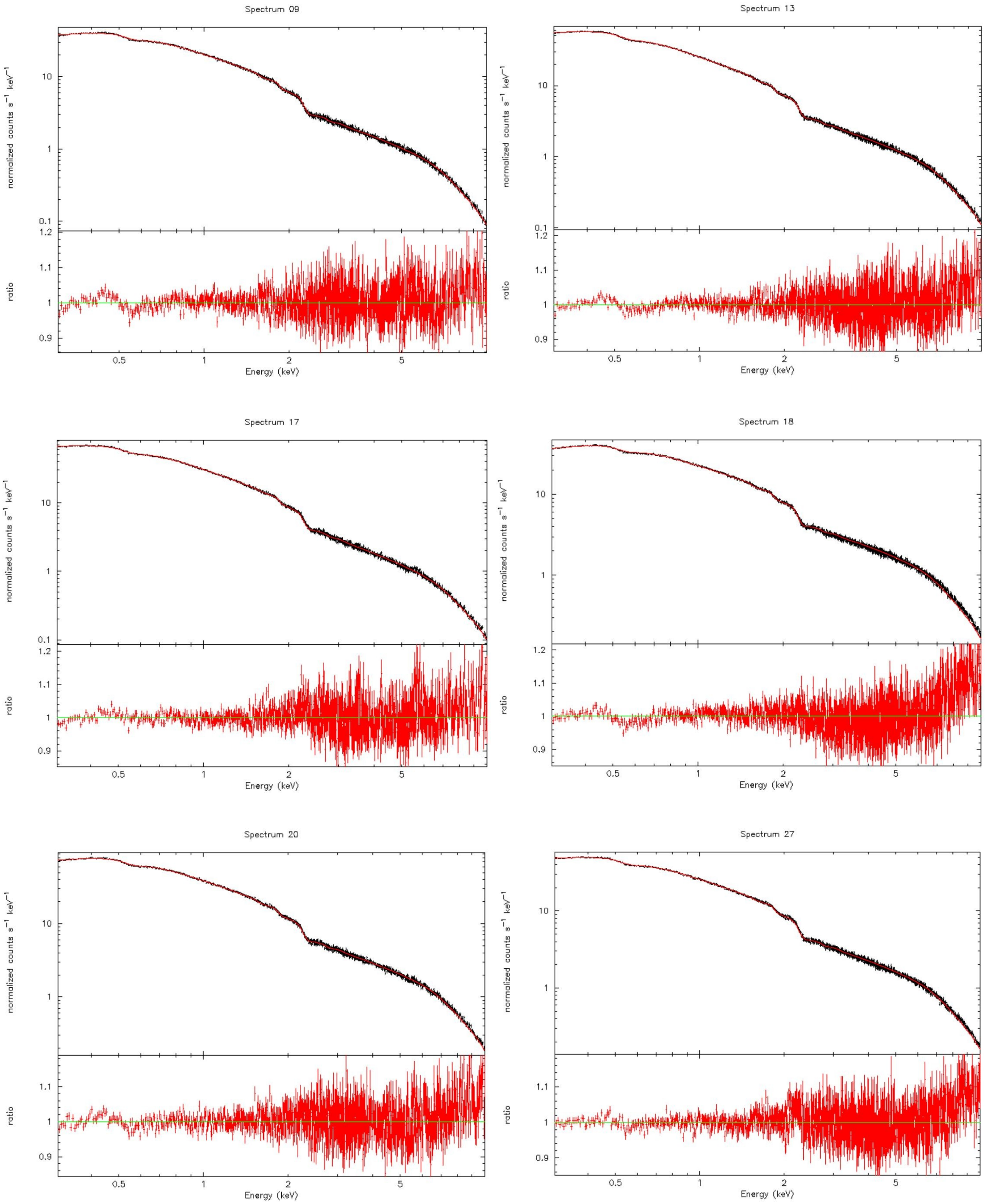

Figure C.5: The jet model fits to the six spectra of 3C273 with upper panel showing the model fitted to data and the lower panel shows the quality of the fit

Bibliography

[1] Stephen Rosswog and Marcus Bruggen, An Introduction to High-Energy Astrophysics, 2007

[2] C. Megan Urry and Paolo Padovani, Unified Schemes for Radio-Loud Active Galactic Nuclei, 1995

[3] William N. Alston et al, A Dynamic Black Hole Corona in an Active Galaxy through X-ray Reverberation Mapping, 2020

[4] B.M. Peterson, The Broad-Line Region in Active Galactic Nuclei, 2006

[5] Braito et al, A High Spectral Resolution Map of the Nuclear Emitting Regions of NGC 7582, 2017

[6] Moshe Elitzur, The Toroidal Obscuration of Active Galactic Nuclei, 2008

[7] Schartmann et al, Towards a Physical Model of Dust Tori in Active Galactic Nuclei, 2005

[8] Kalita el al, Origin of X-rays in the Low State of the FSRQ 3C273: Evidence of Inverse Compton Emission, 2017

[9] Bhatta et al, Hard X-ray Properties of NuStar Blazars, 2018

[10] Alan P. Marscher, Variability of Blazars and Blazar Models over 28 Years, 2016

[11] R.D. Blandford and R.L. Znajek, Electromagnetic Extraction of Energy from Kerr Black Holes, 1977

[12] Livio et al, Extracting Energy from Black Holes: The Relative Importance of the Blandford-Znajek Mechanism, 1998

[13] J.V. Narlikar and S.M. Chitre, Faster-than-Light Motion in Quasars, 1984

[14] Andrea Cottaneo, The Growth History of Giant Black Holes and the Radio Dichotomy of Quasars, 2003

[15] Dennis Gallant, Principle Component Analysis of the X-ray Spectra of Blazars, 2018

[16] XMM-Newton Satellite website:https://www.cosmos.esa.int/web/xmm-newton

[17] Husemann et al, Jet-Driven galaxy-Scale Gas Outflows in the Hyper-Luminous Quasar 3C273

[18] M. Schmidt, 3C 273 : A Star-Like Object with Large Red-Shift, 1963

[19] Kovalev et al, RadioAstron Observations of the Quasar 3C273: A Challenge to the Brightness Temperature Limit, 2016

[20] Page et al 2004, XMM-Newton Observations of 3C273, 2004

[21] G. Ghasellini and F. Tavecchio, Canonical High Power Blazars, 2009

[22] Ghasellini et al, General Physical Properties of bright Fermi blazars, 2010

[23] Emma Gardner and Chris Done, What Powers the Most Relativistic Jets?II: Flat Spectrum Radio Quasars, 2017

[24] UK Swift Data Science Centre, 2013.

[25] Edelson et al, X-Ray Spectral Variability and Rapid Variability of the Soft X-Ray Spectrum Seyfert 1 Galaxies Arakelian 564 and Ton S180, 2001